



#### Available online at www.sciencedirect.com

## **ScienceDirect**

Advances in Space Research 63 (2019) 967-985

ADVANCES IN SPACE RESEARCH (a COSPAR publication)

www.elsevier.com/locate/asr

# Uncertainties in gravity wave parameters, momentum fluxes, and flux divergences estimated from multi-layer measurements of mesospheric nightglow layers

## Fabio Vargas

University of Illinois at Urbana-Champaign, Department of Electrical and Computer Engineering, 306 North Wright Street, 5066 ECEB, MC-702, Urbana, IL 61801, United States

Received 21 March 2018; received in revised form 24 September 2018; accepted 27 September 2018 Available online 3 October 2018

#### **Abstract**

Measurements of dynamic parameters of atmospheric gravity waves, mainly the vertical wavelength, the momentum flux and the momentum flux divergence, are affected by large uncertainties crudely documented in the scientific literature. By using methods of error analysis, we have quantified these uncertainties for frequently observed temporal and spatial wave scales. The results show uncertainties of  $\sim 10\%$ ,  $\sim 35\%$ , and  $\sim 65\%$ , at least, in the vertical wavelength, momentum flux, and flux divergence, respectively. The large uncertainties in the momentum flux and flux divergence are dominated by uncertainties in the Brunt-Väisälä frequency and in spatial separation of the nightglow layers, respectively. The measured uncertainties in fundamental wave parameters such as the wave amplitude, intrinsic period, horizontal wavelength, and wave orientation are  $\sim 10\%$  or less and estimated directly from our nightglow image data set. Other key environmental quantities such as the scale height and the Brunt-Väisälä frequency, frequently considered as constants in gravity wave parameter estimations schemes, are actually quite variable, presenting uncertainties of  $\sim 40\%$  and  $\sim 90\%$ , respectively, according to the several solar activity and seasonal atmosphere scenarios from the NRLMSISE-00 model simulated here.

Keywords: Atmospheric gravity waves; Nightglow; Momentum flux; Momentum flux divergence; Uncertainty estimations; Nightglow imagers

#### 1. Introduction

Atmospheric gravity waves (AGWs) propagate upward from the troposphere to the upper atmosphere, growing in amplitude and causing fluctuations in the background fields (such as the temperature and density) across the mesosphere and lower thermosphere (MLT) region (Hines, 1960). These fluctuations are monitored using several platforms, such as radars, lidars, or satellite systems (e.g., Gardner and Voelz, 1987; Gardner and Taylor, 1998; Batista et al., 2002; Hocking, 2005; Nikoukar et al., 2007; Lu et al., 2009). Observations made from the ground

E-mail address: fvargas@illinois.edu

with all-sky imagers monitor changes in the radiance of the mesospheric nightglows, which are natural traces of the dynamics of atmospheric waves in the MLT (e.g., Krassovsky, 1972; Swenson and Mende, 1994; Reisin and Scheer, 1996; Vargas et al., 2009).

All-sky imagers allow us to record these wave fluctuations in the nightglow with good spatial and temporal resolution (Garcia et al., 1997; Hapgood and Taylor, 1982; Taylor et al., 1997; Li et al., 2011). Because it is a relatively inexpensive but powerful, reliable technique, it has been largely adopted by aeronomers. Wave parameter estimation from images is well-understood and can be carried out with personal computers, which makes all-sky imagery a very convenient and cost-effective tool.

Although several aeronomy groups use imagery to study the AGW dynamics and to report dominant wave characteristics (e.g., Giers et al., 1997; Pautet et al., 2005; Li et al., 2011), the uncertainties of AGW parameters and associated quantities are poorly understood, and only a few studies show explicitly the magnitude of these uncertainties (e.g., Swenson et al., 1999). For example, as environmental changes in the background atmosphere associated with the solar activity and with seasons occur, the determination of the temporal/spatial scales of waves is subject to these unquantified errors, which must be taken into account to estimate other AGW associated quantities in a statistically meaningful manner.

In this study, we have measured and modeled the relative uncertainties in fundamental wave parameters and other critical atmospheric quantities using error analysis theory, aiming to show how these uncertainties propagate into derived, more significant quantities such as the AGW momentum flux and the momentum flux divergence. Based on this approach, we want to show firstly which errors dominate the measurements while discussing viable strategies to minimize these errors, and secondly to show how these significant errors should be thoughtfully estimated for each AGW occurrence.

#### 2. Gravity wave parameters and errors

Nightglow layers are caused by metastable atoms/molecules emitting photons at specific lines/bands near the visible, infrared, or ultraviolet wavelength range (McCormac, 1967; Chamberlain, 1995). Four emission layers (OH, Na,  $O_2(b)$ , and  $O(^1S)$ ) are widely observed in the MLT, having their centroids located at  $\sim$ 89,  $\sim$ 90,  $\sim$ 94, and  $\sim$ 96 km altitude, respectively (Meriwether, 1989; Taylor et al., 1997; Vargas et al., 2007). The different centroid locations permit to observe the characteristics of gravity waves at different altitudes throughout the MLT region.

Short-term fluctuations in the nightglow due to AGWs are the most prominent features present in image records. The waves propagate across the field of view of the imager showing a variety of dynamic characteristics, which can be measured straightforwardly by image processing techniques (e.g., Hapgood and Taylor, 1982; Garcia et al., 1997; Coble et al., 1998; Tang et al., 2005a,b; Li et al., 2011).

We rank the wave parameters in three groups: (i) the first group is composed of wave parameters and their uncertainties estimated from a single image of a single emission; (ii) the second group is composed of wave parameters obtained from a sequence of images of a single layer; (iii) parameters and uncertainties estimated from images of multiple layers form the third group. This differentiation helps to understand the impact of uncertainties of one group into another and points out which uncertainties are more important than others.

We define as fundamental wave parameters the horizontal wavelength  $(\lambda_h)$ , the wave orientation  $(\theta)$ , the wave phase  $(\phi)$ , as well as the wave period  $(\tau)$ , the horizontal phase velocity (c), and the relative wave amplitude (I'), which are directly extracted from the images. The relative wave amplitude is usually given as a percentage of the background nightglow because most imager systems are not calibrated to give the nightglow radiance in absolute units.

For clarity, we also define derived wave parameters as the ones estimated from the AGW linear theory equations that take fundamental and environmental parameters as inputs. The derived parameters are the vertical wavelength  $(\lambda_z)$ , the wave momentum flux (F), and the divergence of the momentum flux (D).

To fully obtain the characteristics of the waves, we must consider environmental parameters such as the spatial separation of two nightglow layers ( $\Delta z$ ), the Brunt-Väisälä frequency (N), the scale height (H), and background mass density ( $\bar{\rho}$ ) or number density ( $[\bar{n}]$ ). The uncertainties associated with each of the AGW quantities are also referred to as fundamental, derived, or environmental, according to the classification rules defined here.

For reference, we have used throughout this text the well-known error propagation formula (e.g., Bevington and Robinson, 1969):

$$\sigma_f^2 = \sum_{i=1}^n \left(\frac{\partial f}{\partial x_i}\right)^2 \sigma_{\bar{x}_i}^2 \tag{1}$$

to estimate the uncertainties in functions such as D and F, assuming that the fundamental wave parameters are uncorrelated. In Eq. (1),  $f = f(x_1, x_2, x_3, \ldots, x_n)$  is a multivariable function, where  $x_i = \bar{x}_i \pm \sigma_{\bar{x}_i}$   $(i = 1, 2, \ldots, n)$  is a random variable, and  $\sigma_{\bar{x}_i}$  is the standard error in  $x_i$ , such as  $\sigma_{\bar{x}_i}^2 = \text{var}(\bar{x}_i) = \frac{1}{N(N-1)} \sum_{i=1}^N (\delta x_i)^2$ ,  $\delta x_i = x_i - \bar{x}_i$ , and  $\bar{x}_i = \frac{1}{N} \sum_{i=1}^N x_i$ .

# 2.1. AGW parameters and errors from a single image of a single nightglow emission

To estimate the uncertainties in the momentum flux and flux divergence, we need first to quantify the uncertainties in the several fundamental parameters which F and D depend upon. This is demonstrated in the next two sections.

The horizontal wavelength, the wave amplitude, and the wave phase are the only parameters fully determined from a single nightglow image. To estimate them, we transform a nightglow image into the horizontal wavenumber domain  $k = 2\pi/\lambda_h = \sqrt{k_x^2 + k_y^2}$  using the two-dimensional Fast Fourier Transform (2DFFT) algorithm (Weeks, 1996), where  $k_x$  and  $k_y$  are the zonal and meridional wavenumbers, respectively. For example, Fig. 1a is an O( $^1S$ ) image recorded at the Andes Lidar Observatory, Chile (30.3°S;

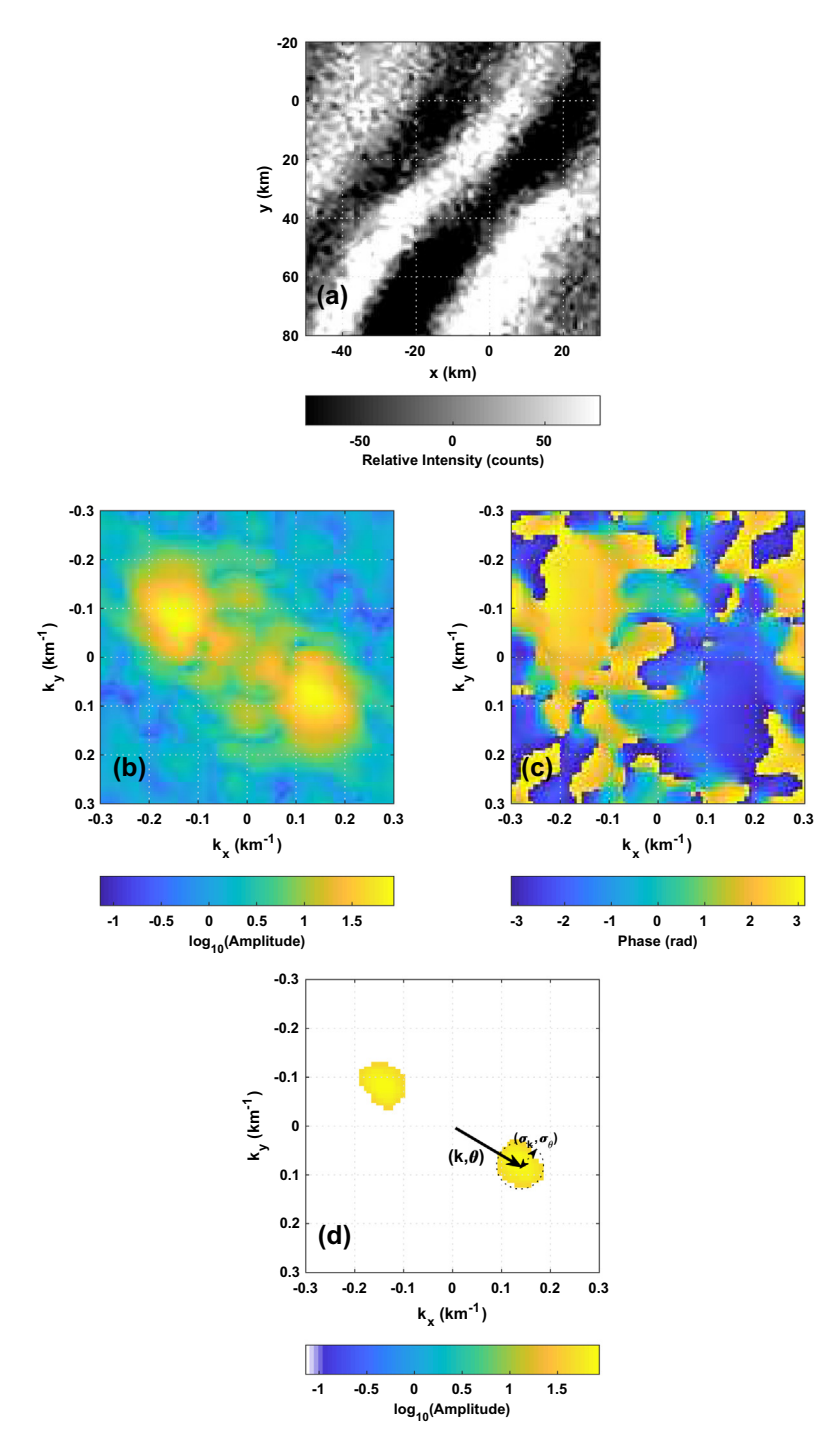


Fig. 1. (a)  $O(^1S)$  image taken at the Andes Lidar Observatory in on Oct 29, 2013, at 05:01:18 UT. (b) 2D horizontal wavenumber amplitude spectra and (c) 2D phase spectra of the image. (d) The selected spectral region in the amplitude spectra (wavenumbers satisfying the 10% condition) to integrate and recover the wave amplitude.

70.7°W) in Oct 28, 2013 at 05:01:18 UT. Fig. 1b and c show respectively the 2DFFT amplitude and phase periodograms of the same nightglow frame.

The image represented in a 2DFFT periodogram is a function of k. An energy peak at  $(k_{xo}, k_{yo})$  in the periodogram allows estimating  $\lambda_h$  and I' unambiguously from the 2DFFT of a single image, while the wave phase comes from the phase periodogram at the point  $(k_{xo}, k_{yo})$ . We

demonstrate how to measure  $\lambda_h$  and I' and their uncertainties  $\sigma_{\lambda_h}$  and  $\sigma_{I'}$  from the 2DFFT as follows.

Larger amplitude, lasting gravity waves recorded in a series of nightglow images materialize in the 2DFFT periodogram as prominent peaks as presented in Fig. 1b (Weeks, 1996). Because of the use of a discrete 2DFFT algorithm, the transformation from the spatial domain into a discrete wavenumber domain does not map exactly,

which translates into a weaker wave energy peak and in leakage of energy from the peak to the neighbor wavenumbers (Hapgood and Taylor, 1982; Hecht et al., 1994; Weeks, 1996; Garcia et al., 1997; Tang et al., 2005b). Small-scale waves are less affected by energy leakage than the large scales because smaller scales comprise a larger number of wavefronts across the field of view, but leakage is never zero.

Fig. 1a presents a  $\sim$ 30 km horizontal wavelength, southeast oriented gravity wave package. The 2DFFT amplitude periodogram of the event in Fig. 1b shows that the longest wavelength of this packet is associated with the innermost, higher power wavenumbers of the periodogram, which also correspond to the strongest wave amplitude. Notice that because of the energy leakage, the wavenumbers surrounding the peak also have high energy, which introduces an uncertainty in the determination of the peak wavenumber, wave orientation, and wave amplitude. Furthermore, because waves interfere with one another, their wavefronts became uneven across the image frame, and because the background wind field acts on the wavefronts and degrades/distorts them, fundamental wave parameters will be subject to these effects as well.

Nightglow images are usually mapped onto a  $512 \times 512 \text{ km}^2$  geographical coordinates grid with a resolution of 1 km/pixel. To minimize the energy leakage in the wavenumber domain, we work with a smaller area of  $170 \times 170 \text{ km}^2$  to carry out the wave amplitude estimation. This  $170 \times 170 \text{ km}^2$  area is large enough to allow the detection of longer horizontal wavelengths, yet small enough to fully encompass the wave fronts in the field of view.

#### 2.1.1. Wave amplitude

The wave amplitude is given by  $I' = \bar{I}' \pm \sigma_{I'}$ , where  $\bar{I}'$  is the result of a two-dimension integration and  $\sigma_{I'}$  is the square root of the nightglow image variance, which we take here as a measured uncertainty in I'. To estimate  $\bar{I}'$ , we integrate around the peak located at  $(k_{xo}, k_{yo})$  (e.g., Coble et al., 1998; Tang et al., 2002). The two-dimension integration domain corresponds to neighbor wavenumbers around the peak presenting energy larger than 10% of the total periodogram energy regardless of the peak shape because it is not necessarily Gaussian. Fig. 1d shows explicitly the integration domain for the example given here (notice the non Gaussian shape of that peak region).

The uncertainty  $\sigma_{I'}$  is estimated from the variance of the nightglow image across the field of view, where usually several interfering waves of various temporal/spatial scales are present. The variance in the field of view is obtained from preprocessed nightglow images (i.e., unwarped, stars removed, geographical coordinates transformed, detrended images), and is a measure of the perturbation caused by all waves, random oscillations, ripples due to instabilities, turbulence, clouds, moonlight contamination, etc., which contribute to wave amplitude uncertainty in a given instant. The variance is convenient here because our image-

processing algorithm relies on the automatic wave detection method.  $\sigma_{I'}$  is usually small if the images' signal to noise ratio is large, and observations are carried out under ideal geophysical conditions (low background contamination caused by the moon or/and city lights) usually give very small uncertainty in the wave amplitude.

#### 2.1.2. Horizontal wavelength

The position of the energy peak in the periodogram defines completely the horizontal wavenumber. However, as energy leaks to the neighbor wavenumbers due to the discretization of the domain, there is an uncertainty in k that can be calculated by averaging the wavenumbers satisfying the 10% condition presented earlier and showed explicitly in Fig. 1d.

The average  $\bar{k}$  is our best experimental estimation of k. The spread in k is evaluated by the standard deviation  $(\sigma_k)$  of the surrounding wavenumbers satisfying the 10% condition. We obtain the standard error  $\sigma_{\bar{k}}$  in k by  $\sigma_k/\sqrt{n}$ , where n is the number of elements in the peak wavenumber region. We finally obtain the horizontal wavelength by  $\lambda_h = 2\pi/\bar{k}$ , and its uncertainty  $\sigma_{\lambda_h}$  by  $\sigma_{\bar{k}}/\bar{k} = \sigma_{\lambda_h}/\lambda_h$ .

# 2.2. AGW parameters and errors from multiple images of a single nightglow emission

Wave parameters such as the wave orientation, the intrinsic period and the horizontal phase velocity are obtained by the combination of sequential images (Hapgood and Taylor, 1982; Garcia et al., 1997; Tang et al., 2002). We demonstrate in this session how to determine these quantities.

#### 2.2.1. Wave orientation

To obtain  $\bar{\theta}$  and  $\sigma_{\theta}$ , we proceed in the same way used to calculate  $\bar{k}$  and  $\sigma_k$  in Section 2.1.2, using instead the expression  $\theta = \tan^{-1}(k_x/k_y)$  to calculate the wave orientation for a given spectral point  $(k_x, k_y)$ , where the north is  $\theta = 0^{\circ}$ . The uncertainty in the wave orientation  $\sigma_{\theta}$  is just the standard deviation of the mean of the  $\theta_i$  set.

Even the propagation direction of a given wave obtained from the image spectrum still presents an intrinsic 180° ambiguity that must be dealt with to find the actual orientation. The easiest way to solve the ambiguity for a single wave event is by observing the wave progression across the field of view in subsequent images via animation of the image set.

#### 2.2.2. Wave period

Since we are also interested in the temporal scales of AGWs, we calculate the wave period from:

$$\tau = \frac{\lambda_h}{c},\tag{2}$$

and its uncertainty by:

$$\sigma_{\tau}^{2} = \left(\frac{\tau}{\lambda_{h}}\right)^{2} \sigma_{\lambda_{h}}^{2} + \left(\frac{\tau}{c}\right)^{2} \sigma_{c}^{2} \tag{3}$$

To obtain the wave frequency  $(\omega)$  and the wave frequency uncertainty  $(\sigma_{\omega})$ , we use, respectively,  $\omega = 2\pi/\tau$  and  $\sigma_{\tau}/\tau = \sigma_{\omega}/\omega$ .

#### 2.2.3. Horizontal phase velocity

The horizontal phase velocity (c) in Eq. (2) is given by:

$$c = \frac{\lambda_h}{2\pi} \frac{\Delta \phi}{\Delta t} \tag{4}$$

where  $\Delta \phi$  represents the wave phase lag measured from the cross periodogram of two sequential images of the same emission for the spectral peak at  $(k_x, k_y)$ . Using the general error equation, we show that the variance associated with c is:

$$\sigma_c^2 = \left(\frac{c}{\lambda_h}\right)^2 \sigma_{\lambda_h}^2 + \left(\frac{c}{\Delta \phi}\right)^2 \sigma_{\Delta \phi}^2 + \left(\frac{c}{\Delta t}\right)^2 \sigma_{\Delta t}^2 \tag{5}$$

where  $\sigma_{\lambda_h}^2$ ,  $\sigma_{\Delta\phi}^2$ , and  $\sigma_{\Delta t}^2$  correspond to variances in  $\lambda_h$ ,  $\Delta\phi$ , and  $\Delta t$ , respectively.

Fig. 2 shows a plot of c vs.  $\Delta \phi$  calculated with Eq. (4) for various acquisition times and a horizontal wavelength of 100 km, which is a typical scale of waves observed in nightglow images. The thick black line in Fig. 2 refers to the acquisition time used in our imaging system, which

records images of the OH and O( $^1S$ ) emissions with integration times of 60 s and 90 s, respectively, and translates in  $\Delta t = 2.5$  min time interval between images of a single emission. The numerical range indicated on the vertical and horizontal axes in Fig. 2 were extrapolated once realistic AGW phase velocities range from  $\sim 30$  m/s to  $\sim 150$  m/s, corresponding to the smaller phase lag range only ( $\Delta \phi < 1.47$ rad =  $85^\circ$ ). Notice that as the acquisition time decreases, larger velocity ranges can be assessed. However, occurrences of waves presenting c > 100 m/s are sparser.

#### 2.2.4. Vertical wavelength, 1st approach

The vertical wavenumber (m) is obtained from the dispersion relation that is derived in the linear theory of gravity waves (Hines, 1960; Nappo, 2012). The complete AGW dispersion relation is given by:

$$m^{2} = \frac{(N^{2} - \omega^{2})}{(\omega^{2} - f^{2})} k^{2} + \frac{\omega^{2}}{c_{s}^{2}} - \frac{1}{4H^{2}}$$
 (6)

where f is the inertial frequency, and  $c_s$  is the sound speed. Notice that Eq. (6) neglects the terms of wind shear and curvature that has no consequence to the present analysis once the frequency shift is corrected prior to apply Eq. (6) to obtain the vertical wavenumber. Moreover, Since it is not feasible to observe acoustic waves using our multilayer nightglow imaging systems, due to exposure times

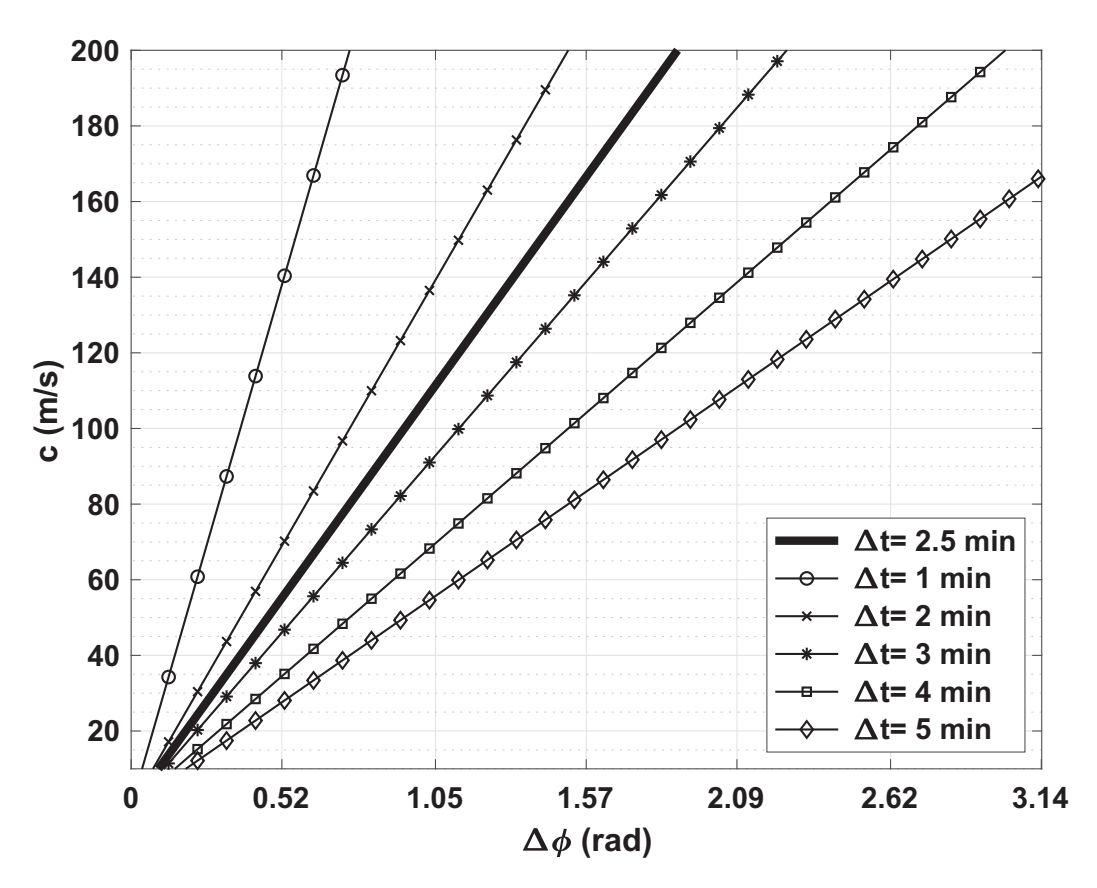


Fig. 2. Horizontal phase velocity versus  $\Delta \phi$  for  $\lambda_h = 100$  km and various acquisition times  $\Delta t$ .

and cadences that limit time resolution, we can use the Boussinesq approximation to simplify Eq. (6) to:

$$m^2 = \left(\frac{N^2}{\omega^2} - 1\right)k^2 - \frac{1}{4H^2} \tag{7}$$

This simpler relationship neglects acoustic waves, yet holds the compressibility term  $1/4H^2$  that is important for high frequency gravity waves ( $\omega \gg f$ ), which are still subject to compressibility effects (see Nappo, 2012).

The uncertainty in m using Eq. (7) is then:

$$\sigma_m^2 = \left(-\frac{N^2 k^2}{m\omega^3}\right)^2 \sigma_\omega^2 + \left(\frac{k}{m} \left[\frac{N^2}{\omega^2} - 1\right]\right)^2 \sigma_k^2 + \left(\frac{Nk^2}{m\omega^2}\right)^2 \sigma_N^2 + \left(\frac{1}{4mH^3}\right)^2 \sigma_H^2$$
(8)

To obtain the vertical wavelength and the vertical wavelength uncertainty we use, respectively,  $m=2\pi/\lambda_z$  and  $\sigma_m/m=\sigma_{\lambda_z}/\lambda_z$ .

#### 2.2.5. Environmental quantities

The m variance depends upon environmental parameters such as N and H, which are usually assumed as con-

stants in many AGW studies. To understand the changes and the uncertainties in these and other environmental parameters, we have used the NRLMSISE-00 model (Picone et al., 2002) to assess the background thermal and compositional structure of the atmosphere for different seasons and for distinct solar activity conditions. Notice that by using the NRLMSISE-00 model here we intend to demonstrate our method of analysis and to show the magnitude of the uncertainties in some gravity wave parameters. However, the uncertainties presented here would be reduced if, for instance, actual and accurate data from lidars and satellites were used as inputs in this modeling.

The set of environmental parameters of interest for our calculations are the total number density ([n]), the atomic oxygen number density ([O]), the temperature (T), the Brunt-Väisälä frequency (N), and the scale height (H). Observe that [n] and [O] are used ahead in our model to compute the variability of the cancellation factor that is incorporated in the calculation of the AGW momentum flux F, as discussed later in this paper.

Fig. 3a shows the total number density and Fig. 3b the atomic oxygen number density in the range of 75–110 km

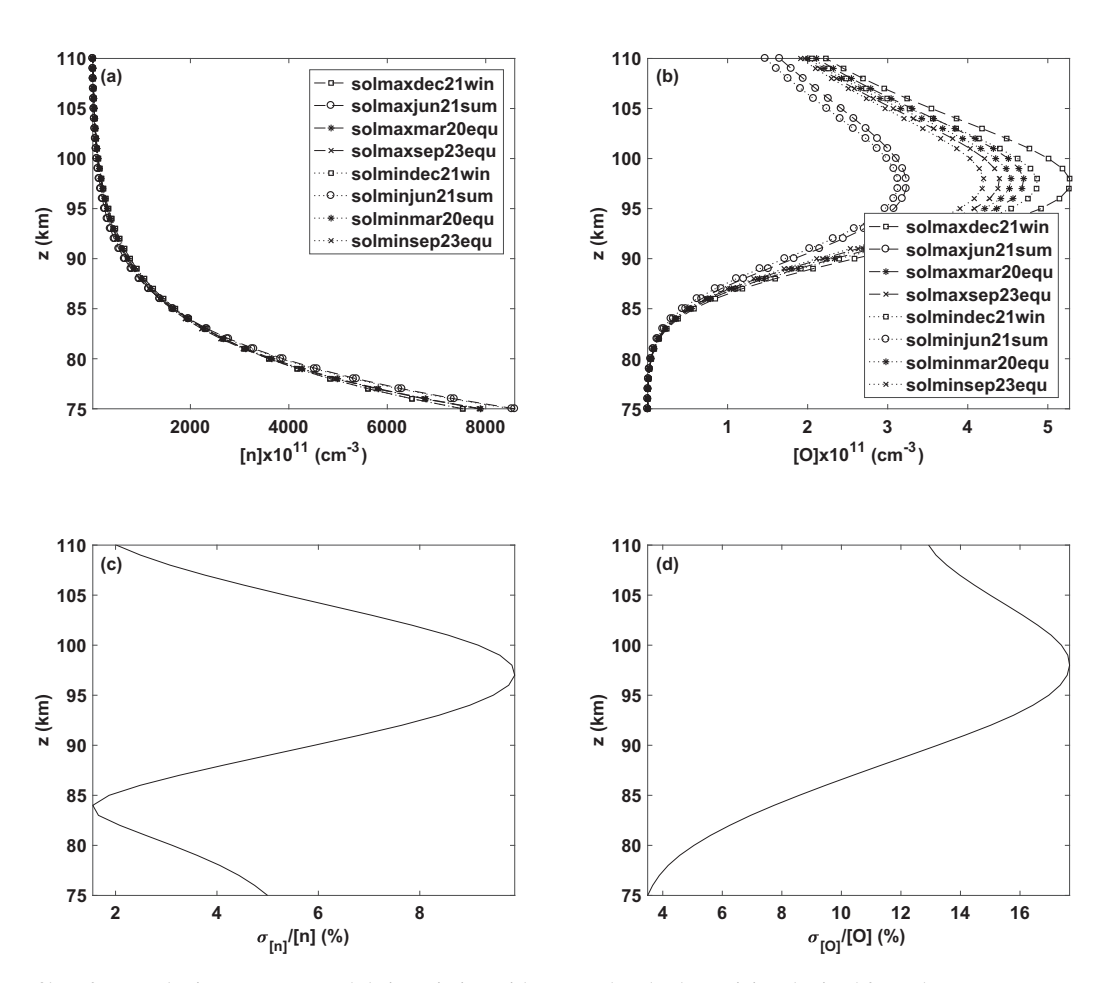


Fig. 3. Vertical profiles of atmospheric parameters and their variation with seasonal and solar activity obtained from the NRLMSISE-00 model. (a) shows the numerical density, (b) the atomic oxygen density, (c) the numerical density relative uncertainty, and (d) the atomic oxygen relative uncertainty. These vertical profiles were calculated for the Andes Lidar Observatory location at (30.3°S,70.7°W).

for eight environmental conditions, i.e., solar maximum summer/winter solstices, solar maximum vernal/autumnal equinoxes, solar minimum summer/winter solstices, and solar minimum vernal/autumnal equinoxes. Note quite a change in both densities as the atmosphere experiences different solar/seasonal conditions.

Fig. 3c and d show, respectively, the relative uncertainty in [n] and [O] calculated from the variance formula. Notice these uncertainties have distinct magnitudes in different altitudes. For instance,  $\sigma_{[O]}/[O]$  is large about the  $O(^1S)$  peak altitude ( $\sim$ 96 km), and is maximum right above the peak ( $\sim$ 16%). This has a profound impact on the cancellation factor magnitude and its uncertainty, which critically depend upon the atomic oxygen density in a given altitude (e.g., Swenson and Gardner, 1998).

Observe that the realistic oxygen number density would change quite much in altitude and in longitude according to observational data (Offermann et al., 1981; Shepherd et al., 1993). The atomic oxygen density provided by the NRLMSISE-00 model serves here only as an estimate of the actual [O] variability, which is ultimately controlled by tides and planetary waves, gravity wave breaking, solar

cycle, and downward flux of O from the lower thermosphere (e.g., Swenson et al., 2018).

The geophysical changes in H and N are shown in Fig. 4a and b, respectively. We took the temperature provided by the NRLMSISE-00 to obtain the magnitudes of H and N in the MLT range.

The scale height is obtained by using H = RT/g, where R = 287.05 J/kg/K is the specific gas constant. This formula takes into account that the air is well mixed below the turbopause and that the mean molecular weight does not change critically with altitude. The scale height depends upon the temperature profile only, and serves as a proxy of the thermal structure of the MLT.

To obtain N for the atmospheric conditions simulated here, we have used the expression  $N^2=(g/T)(dT/dz+g/c_p)$ , where  $g/c_p=9.8$  K/km is the adiabatic lapse rate,  $c_p$  the specific heat at constant pressure, g the acceleration due to the gravity, and dT/dz is the environmental lapse rate. The Brunt-Väisälä frequency depends upon both the atmosphere temperature and the temperature gradient, and wherever the environmental lapse rate is less than the

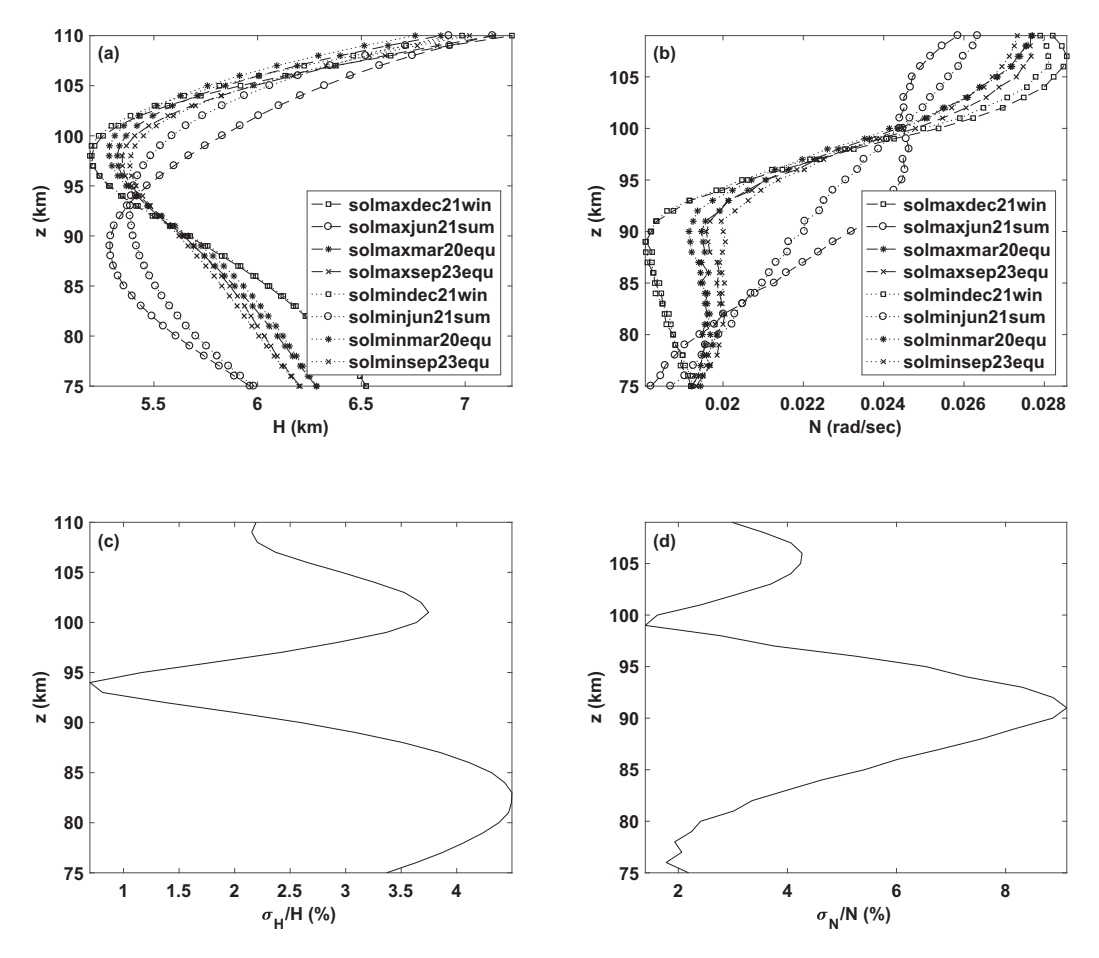


Fig. 4. Vertical profiles of background atmospheric parameters and their seasonal and solar activity variation from the NRLMSISE-00 model. The temperature (not shown) provided by the model was used to estimate H and N in the MLT. (a) shows scale height, (b) the Brunt-Väisälä frequency, (c) the scale height relative uncertainty, and (d) the Brunt-Väisälä frequency relative uncertainty. These vertical profiles were calculated for the Andes Lidar Observatory location at  $(30.3^{\circ}S, 70.7^{\circ}W)$ .

adiabatic lapse rate, we observe a convective unstable atmosphere.

The uncertainties of H and N are in Fig. 4c and d, respectively. Differently than what is assumed in many studies, the changes in H and N are substantial. For instance, the relative error  $\sigma_N/N$  ranges from  $\sim 2\%$  at 80 km to more than 8% at about the OH centroid altitude (Fig. 4d), which is relatively large for a parameter frequently assumed as constant. Because of these substantial changes, we must consider their magnitudes and uncertainties separately at each layer centroid altitude in order to obtain a better estimation of  $\lambda_z$ , F, and D, for instance.

#### 2.2.6. Momentum flux

The momentum flux is one of the most important wave quantities obtained from nightglow imaging. The gravity wave momentum flux *F* is interesting because it is a measure of the gravity wave forcing in the MLT (e.g., Swenson and Liu, 1998; Swenson et al., 1999; Liu and Swenson, 2003; Vargas et al., 2007). The momentum flux per unit mass is given by:

$$F = \langle w'u' \rangle = -\frac{1}{2} \frac{g^2}{N^4} \frac{m}{k} \omega^2 \left(\frac{I'}{CF}\right)^2 \tag{9}$$

where w' wave vertical wind perturbation, u' represents the horizontal wind perturbation towards the wave propagation direction,  $m=2\pi/\lambda_z$  the vertical wavenumber,  $k=2\pi/\lambda_h$  the horizontal wavenumber,  $\omega=2\pi/\tau$  the angular wave frequency, N the Brunt-Väisälä frequency, and I' the relative wave amplitude. Moreover, the acceleration due to the gravity g is taken as a function of altitude in our calculations, and CF is the cancellation factor as modeled by Swenson and Gardner (1998), Swenson and Liu (1998), Liu and Swenson (2003), Vargas et al. (2007). The momentum flux is then evaluated individually for each wave event perturbing a given nightglow layer.

Using the general error equation, we obtain the variance of F as a function of seven uncertainties associated with each variable in Eq. (9) as follow:

$$\sigma_F^2 = \left(\frac{F}{m}\right)^2 \sigma_m^2 + \left(\frac{2F}{\omega}\right)^2 \sigma_\omega^2 + \left(\frac{2F}{I'}\right)^2 \sigma_{I'}^2 + \left(\frac{F}{k}\right)^2 \sigma_k^2 + \left(\frac{2F}{CF}\right)^2 \sigma_{CF}^2 + \left(\frac{4F}{N}\right)^2 \sigma_N^2$$

$$(10)$$

where the  $\sigma^2$  represent the variance of each parameter. The variances  $\sigma_{\omega}^2$ ,  $\sigma_A^2$ , and  $\sigma_k^2$  are obtained directly from night-glow images, while  $\sigma_{CF}^2$  and  $\sigma_N^2$  must be obtained from models (e.g., Picone et al., 2002), from resonance temperature/wind lidar data, or from satellite measurements when they are available.

#### 2.2.7. Cancellation factor

The cancellation factor in Eq. (9) is defined as  $CF = (I'/\overline{I})/(T'/\overline{T})$ , where primed quantities refer to the wave fluctuation, and bar quantities to the unperturbed

background. *CF* is valuable to retrieve the magnitude of the relative temperature fluctuation in terms of that in the nightglow radiance fluctuation, which is used to estimate the momentum flux magnitude transported by the wave

The magnitude of the cancellation factor CF is also estimated for different solar and seasonal conditions, as the atomic oxygen density changes dramatically under different solar/seasonal atmospheric states. The CF magnitude for each of these different environmental scenarios has been assessed by using the Vargas et al. (2007) model with the input of different background conditions provided by the NRLMSISE-00 model. The results are presented in Fig. 5a (Fig. 5b) for the  $O(^1S)$  (OH) emission. The mean CF for each emission (continuous thick line) is obtained by fitting the following model to the several curves:

$$CF = a_1 - a_2 e^{-a_3 \lambda_z} \tag{11}$$

where  $a_1, a_2$  and  $a_3$  are fitting coefficients also subject to uncertainties that must be specified for each nightglow layer, and  $\lambda_z$  is the vertical wavelength. As we assume that each term in Eq. (11) is variable, the error in CF is:

$$\sigma_{CF}^{2} = \left(a_{2}a_{3}e^{-a_{3}\lambda_{z}}\right)^{2}\sigma_{\lambda_{z}}^{2} + \sigma_{a_{1}}^{2} + \left(e^{-a_{3}\lambda_{z}}\right)^{2}\sigma_{a_{2}}^{2} + \left(a_{2}\lambda_{z}e^{-a_{3}\lambda_{z}}\right)^{2}\sigma_{a_{2}}^{2}$$

$$(12)$$

Values of each fitting coefficient and their uncertainties  $\sigma_{a_1}$ ,  $\sigma_{a_2}$ , and  $\sigma_{a_3}$  are given in Table 1 for each emission. The uncertainty  $\sigma_{\lambda_z}$  is estimated by evaluating Eq. (8) for a hypothetical wave. The continuous thin lines in Fig. 5 represent the 95% confidence bounds around the fitted curve (continuous thick line). Note that the uncertainty in *CF* for the OH is larger than that in  $O(^1S)$  because of the higher oxygen number density gradient near the OH centroid altitude, as shown in Fig. 3b (Vargas et al., 2007).

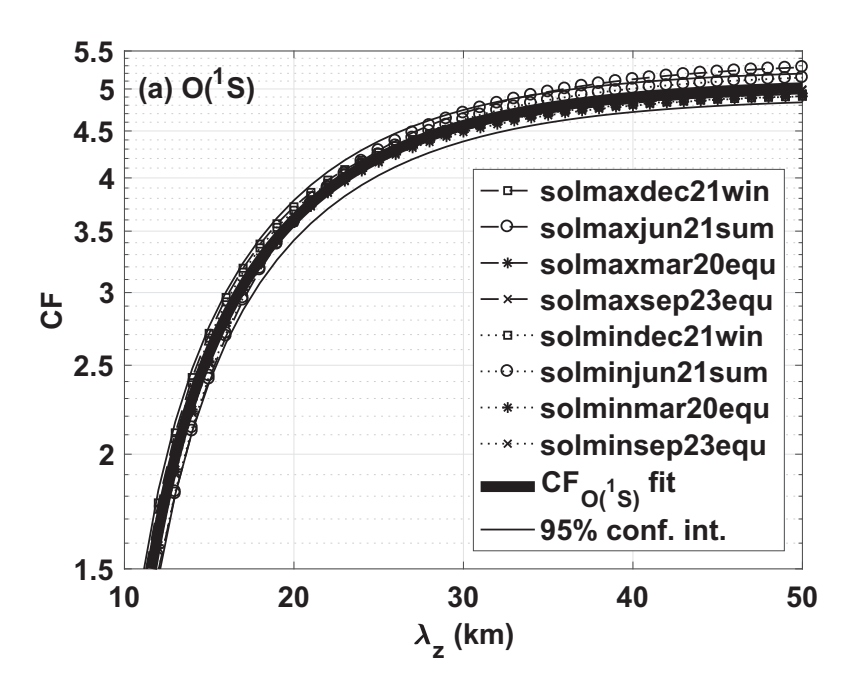
The error in CF is dominated by the error in  $\lambda_z$ . To demonstrate this, we set  $\sigma_{a_1} = \sigma_{a_2} = \sigma_{a_3} = 0$  to show from Eq. (6) that:

$$\frac{\sigma_{CF}}{\sigma_{\lambda_z}} = a_2 a_3 e^{-a_3 \lambda_z} \tag{13}$$

Notice that the uncertainty gets larger (smaller) as the vertical wavelength gets smaller (larger). Also, on the small wavelength range the relative error in CF is larger for the  $O(^1S)$  than that for the OH emission, but  $\sigma_{CF}/\sigma_{\lambda_z}$  approaches zero for both emissions as  $\lambda_z$  gets larger than 50 km. These effects are presented in Fig. 6 for each emission using the coefficients in Table 1.

# 2.3. AGW parameters and errors from multiple images of multiple nightglow emissions

The idea behind measuring AGW parameters from multiple layer observations is to understand how their perturbations are transmitted across the mesosphere region. For instance, a wave amplitude decreasing with altitude would indicate dissipation and wave forcing in the region.



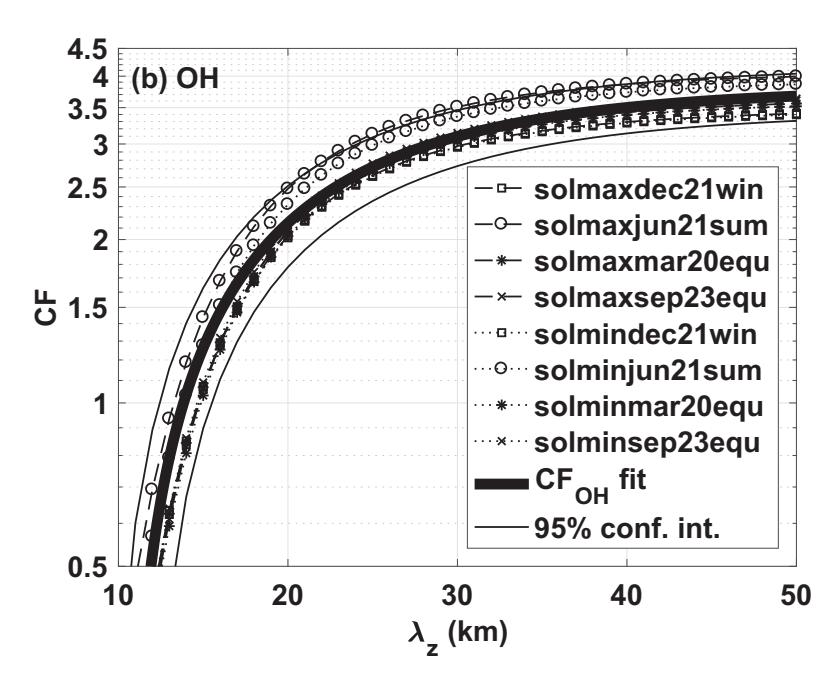


Fig. 5. Modeled cancellation factor for (a)  $O(^1S)$  and (b) OH layers taking into account several solar and seasonal conditions. Continuous thin lines indicate the 95% confidence intervals of the fitting. Input profiles used here to obtain CF were taken from the NRLMSISE-00 for the Andes Lidar Observatory location at (30.3°S,70.7°W).

Table 1 Fitting coefficients of Eq. (11) and their uncertainties.

	ОН	$O(^1S)$
$a_1 \pm \sigma_{a_1}$	$3.800 \pm 0.030$	$5.078 \pm 0.011$
$a_2 \pm \sigma_{a_2}$	$9.12 \pm 0.23$	$12.16 \pm 0.16$
$a_3 \pm \sigma_{a_3}$	$0.0852 \pm 0.0023$	$0.1054 \pm 0.0012$

Wave forcing estimated from the flux divergence measurements represents an important quantity that can be made only by observing the wave perturbation in multiple nightglow layers simultaneously in both of them (e.g., Vargas et al., 2007, 2009, 2015).

Most aeronomy groups use imagers with multiple filters having center frequencies and line widths suitable to make nightglow measurements. OH and  $O(^1S)$  images have finite exposure times which must be considered. The OH filter has a larger bandwidth and requires shorter exposure time ( $\sim$ 60 s) to produce images with good signal to noise ratio. The  $O(^1S)$  emission line is fainter and requires a narrow linewidth filter. Because of that, the  $O(^1S)$  emission is

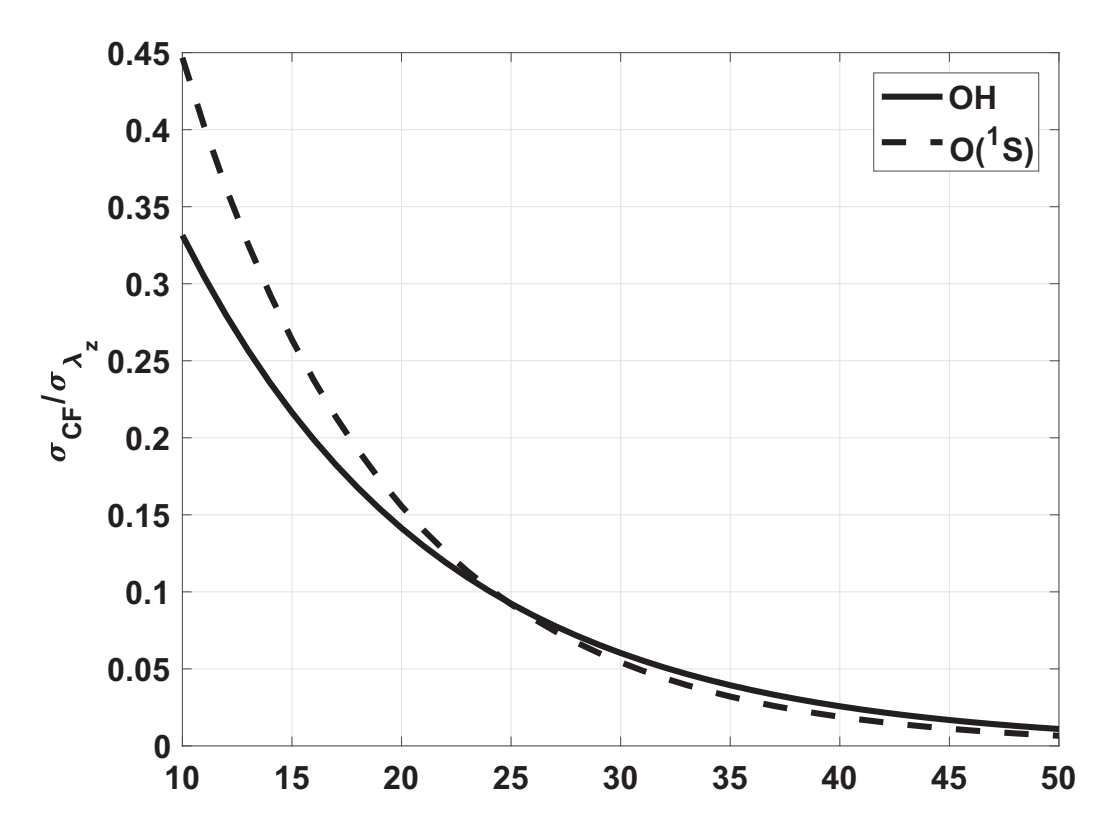


Fig. 6. Relative uncertainty in CF as a function of the vertical wavelength.

observed using longer exposure time ( $\sim$ 90 s). Thus, this two-filter imager system requires 2.5 min to complete one cycle, which sets up the acquisition time. This system barely resolves waves with frequencies near N, and the addition of more filters in the system will just worsen the resolving capability. However, while using multiple filters degrades the temporal resolution, it is the only way to access key MLT information, such as the flux divergence via multiple nightglow observations.

#### 2.3.1. Momentum flux divergence

The momentum flux divergence D is another key parameter obtained from observing the AGW dynamics through the nightglow imagery and represents directly the drag forcing (or acceleration) in the mesosphere region due to breaking and dissipating gravity waves. The flux divergence is given by:

$$D = -\frac{1}{\bar{\rho}} \frac{\partial (\bar{\rho}F)}{\partial z} = -\frac{1}{\bar{\rho}} \left( \frac{\partial \bar{\rho}}{\partial z} F + \frac{\partial F}{\partial z} \bar{\rho} \right) \tag{14}$$

where  $D = d\bar{u}/dt$  and  $F = \langle w'u' \rangle$  are the flux divergence and the momentum flux towards the wave orientation  $\theta = \bar{\theta} \pm \sigma_{\theta}$ , respectively, and  $\bar{\rho}$  is the background density. Measurements of D from imagery are achieved only by recording images of two nightglow layers simultaneously as demonstrated in Vargas et al. (2015). A comprehensive modeling of D for several vertical wave scales and dissipation scenarios is found in Vargas et al. (2007).

Approximating Eq. (14) by its finite difference counterpart we obtain:

$$D \approx -\frac{1}{\bar{\rho}} \left( \frac{\Delta \bar{\rho}}{\Delta z} F + \frac{\Delta F}{\Delta z} \bar{\rho} \right) \tag{15}$$

where  $\Delta F$  is the momentum flux difference between the top and bottom nightglow layers,  $\Delta z$  is the separation of the layers relative to their centroids, and  $\Delta \bar{\rho}$  is the background density difference between those two altitude levels. The other quantities  $\bar{\rho}$  and F are the background density and the wave momentum flux evaluated at a given reference level between the layers. For simplicity, we chose  $z_r = 87$  km as the reference level, which coincides with the centroid of the OH emission. Also, we have assumed  $\Delta z = 7$  km based on the results of Vargas et al. (2007). Every parameter in Eq. (15) is subject to uncertainties as discussed earlier in this paper.

The error in Eq. (15) is obtained by differentiating D respect to the independent variables to obtain:

$$\begin{split} \sigma_{D}^{2} &= \left(\frac{\Delta \bar{\rho}}{\bar{\rho}} \frac{F}{\Delta z^{2}} + \frac{\Delta F}{\Delta z^{2}}\right)^{2} \sigma_{\Delta z}^{2} + \left(\frac{1}{\Delta z}\right)^{2} \sigma_{\Delta F}^{2} \\ &+ \left(\frac{1}{\bar{\rho}} \frac{F}{\Delta z}\right)^{2} \sigma_{\Delta \bar{\rho}}^{2} + \left(\frac{1}{\bar{\rho}} \frac{\Delta \bar{\rho}}{\Delta z}\right)^{2} \sigma_{F}^{2} + \left(\frac{\Delta \bar{\rho}}{\bar{\rho}^{2}} \frac{F}{\Delta z}\right)^{2} \sigma_{\bar{\rho}}^{2} \end{split} \tag{16}$$

where the partial derivatives must be evaluated at  $z = z_r$  as well.

### 2.3.2. Vertical wavelength, 2nd approach

Beyond the flux divergence, we can also measure the vertical wavelength by observing two distinct layers. The vertical wavelength  $\lambda_z$  obtained via multiple airglow measurements does not utilize the dispersion relation and can be used to validate the results from Eq. (7).

The magnitude of  $\lambda_z$  using this alternative approach is a function of the layer separation and the wave phase lag, as long the wave is observed simultaneously in both of them. Thus, we can write:

$$\lambda_z = 2\pi \frac{\Delta z}{\Delta \phi} \tag{17}$$

where phase lag  $\Delta \phi = \phi_2 - \phi_1$ .  $\phi_2$  and  $\phi_1$  are the wave phase at the centroid of the top and at the bottom layers, respectively.

Fig. 7 shows curves of Eq. (17) evaluated for several separations of the OH and O( $^1S$ ) layers. The range of the vertical axis is exaggerated in this figure once observational data reveal  $\lambda_z < 100$  km for  $\Delta \phi > 0.52$  rad = 30° only.

The inherent uncertainty in  $\lambda_z$  in this approach is given by:

$$\sigma_{\lambda_z}^2 = \left(\frac{\lambda_z}{\Delta z}\right)^2 \sigma_{\Delta z}^2 + \left(\frac{\lambda_z}{\Delta \phi}\right)^2 \sigma_{\Delta \phi}^2 \tag{18}$$

where  $\sigma_{\Delta z}^2$  is based on results of Zhao et al. (2005), and  $\sigma_{\Delta \phi}^2$  is obtained directly from the uncertainty of the observed wave phase lag between the top and the bottom layers.

#### 3. Results

To make a useful estimation of AGW parameter uncertainties, we have evaluated the equations in Section 2 using

typical gravity wave temporal/spatial scales obtained from our nightglow observations. These typical AGW scales resemble those of high frequency, fast phase speed perturbations, which are compatible with the simplified dispersion relation (Eq. (7)). As shown in detail in Section 2.2, environmental quantities such as N and H were obtained for a distinct season and solar activity scenarios with the aid of the NRLMSISE-00 model.

#### 3.1. Single layer measurement uncertainties

From our nightglow image database, we have estimated the uncertainties on the fundamental AGW parameters  $\lambda_h$ ,  $\theta$ , and I' using the methods established, while the uncertainty in  $\tau$  is given by Eq. (3). Fig. 8 shows these four quantities plotted against their respective uncertainties estimated for waves recorded during 10 days of observations of the OH emission at the Andes Lidar Observatory (30.30°S, 70.7°W). These measured fundamental parameters and their uncertainties, as well as the modeled environmental quantities N and H and their uncertainties, are inputs in the equations developed in Section 2.

Fig. 8a and d present the relative uncertainty in  $\lambda_h$  and in  $\tau$ , respectively. Fig. 8a shows that the relative error  $\sigma_{\lambda_h}/\lambda_h$  increases as  $\lambda_h$  increases. Likewise, the uncertainty  $\sigma_{\tau}$  also increases with  $\tau$  (Fig. 8d), because  $\tau$  depends on  $\lambda_h$  and  $\sigma_{\tau}$  depends on  $\sigma_{\lambda_h}$ . However,  $\sigma_{\tau}$  has a higher spread than  $\sigma_{\lambda_h}$  because of the  $\sigma_c$  term in Eq. (3).

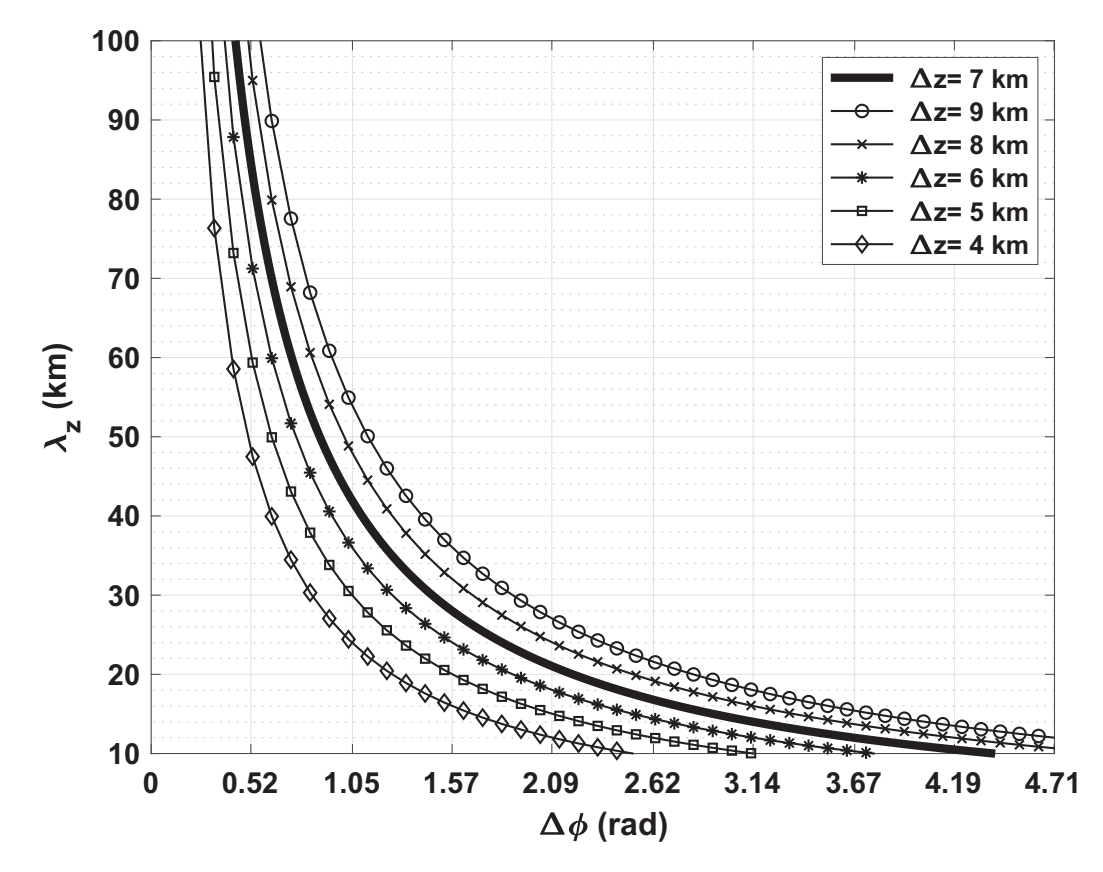


Fig. 7.  $\lambda_z$  dependency on  $\Delta\phi$  assuming different layers' separation values.  $\Delta z = 7$  km is the layer separation used in this work.

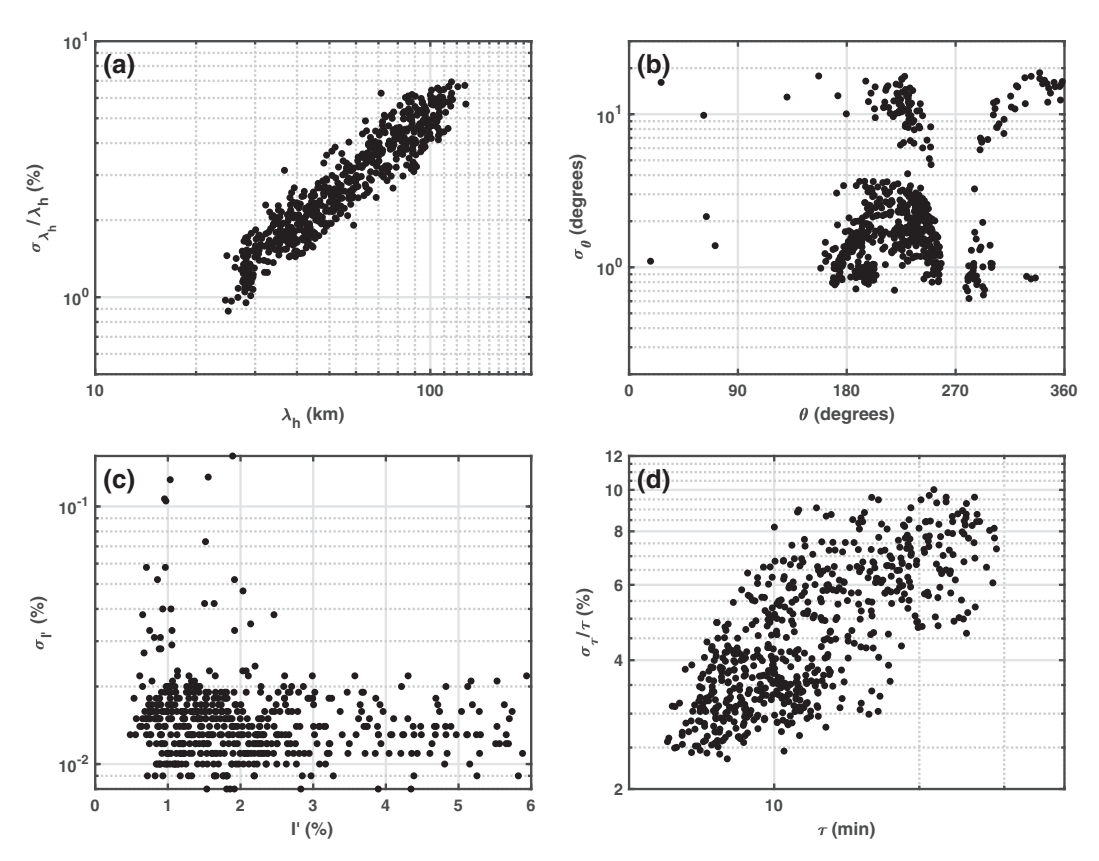


Fig. 8. Primary AGW parameters and their uncertainties obtained from OH nightglow images recorded at the Andes Lidar Observatory in February 2014. (a) shows the horizontal wavelength against its relative uncertainty, (b) the wave orientation against its absolute uncertainty, (c) the wave amplitude against its relative uncertainty, and (d) the wave period against its relative uncertainty. The perturbation I' and its uncertainty are given as a percentage of the background nightglow radiance.

Absolute uncertainty in the wave orientation and amplitude are presented in Fig. 8b and c, respectively. The absolute uncertainty in  $\theta$  (Fig. 8b) is smaller than 30°, and the larger uncertainty values are associated with larger wavelengths according to our measurements of  $\lambda_h$  and  $\theta$  from ALO nightglow images. Fig. 8c shows that the bulk of wave amplitudes falls in the range of 0% to 3%, while their uncertainties are small, ranging from 0.01% to 0.1%. Yet, smaller wave amplitudes present larger uncertainties.

Fig. 9 presents the relative uncertainty  $\sigma_{\lambda_z}/\lambda_z$  as a function of  $\sigma_{\lambda_h}/\lambda_h$  and  $\sigma_{\tau}/\tau$  (see Eq. (8)) for the O( $^1S$ ) and OH emissions. The variation range of  $\sigma_{\lambda_h}/\lambda_h$  and  $\sigma_{\tau}/\tau$  (from 0 to 0.3) is quite large compared to their relative variation in actual data (Fig. 8a and d, respectively). For the simulated conditions here, however, the relative error in  $\lambda_z$  can be as large as ~55%, depending on the layer. Also, notice that  $\sigma_{\lambda_z}/\lambda_z$  does not go to zero when the relative uncertainties in  $\lambda_h$  and  $\tau$  go to zero, because  $\sigma_N$  and  $\sigma_H$  are nonzero (see Eq. (8)).

Fig. 10 shows the momentum flux uncertainty from Eq. (10) in terms of relative errors in  $\lambda_h$  and  $\tau$  as well. Notice that  $\sigma_F/F$  varies faster in the direction of  $\sigma_\tau/\tau$ , which reflects the dependency of F on  $\omega^2$  (see Eq. (9)). Also, the error in F is nonzero even when the relative errors in  $\lambda_h$  and  $\tau$  are zero, because the relative uncertainty in the wave

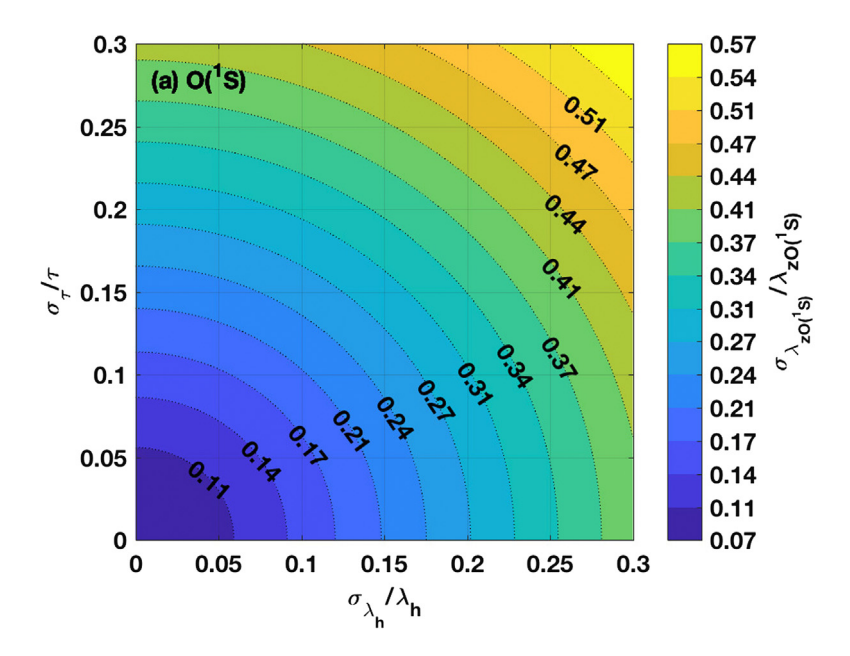
amplitude, vertical wavelength, cancellation factor, Brunt-Väisälä frequency, and scale height are nonzero. We can individually turn on/off these error sources in our simulation to understand how the overall F uncertainty depends upon individual uncertainties. This is discussed ahead in Section 4.

#### 3.2. Multiple layer measurement uncertainties

The uncertainty in the flux divergence (Fig. 11) depends upon several wave parameters that are distinct for each layer because background atmospheric changes throughout the MLT. To compose Fig. 11, we have considered a saturated wave that has the same amplitude at the top and at the bottom layers. As the divergence is calculated from the momentum flux, it has also a dependency on  $\sigma_{\lambda_h}/\lambda_h$  and  $\sigma_{\tau}/\tau$ , and is also nonzero even when  $\sigma_{\lambda_h}$  and  $\sigma_{\tau}$  go to zero.

Because of the geophysical differences of all the background quantities whose  $\sigma_D$  depends upon, and because of the D uncertainty ranges widely  $(0.6 \lesssim \sigma_D/D \lesssim 0.9)$ , we would anticipate huge difficulties in measuring the flux divergence via nightglow data, at least in the experimental circumstances modeled here.

In Fig. 12, to study how the uncertainty in  $\lambda_z$  varies due to  $\sigma_{\Delta\phi}$  and  $\sigma_{\Delta z}$  using the alternative scheme represented by



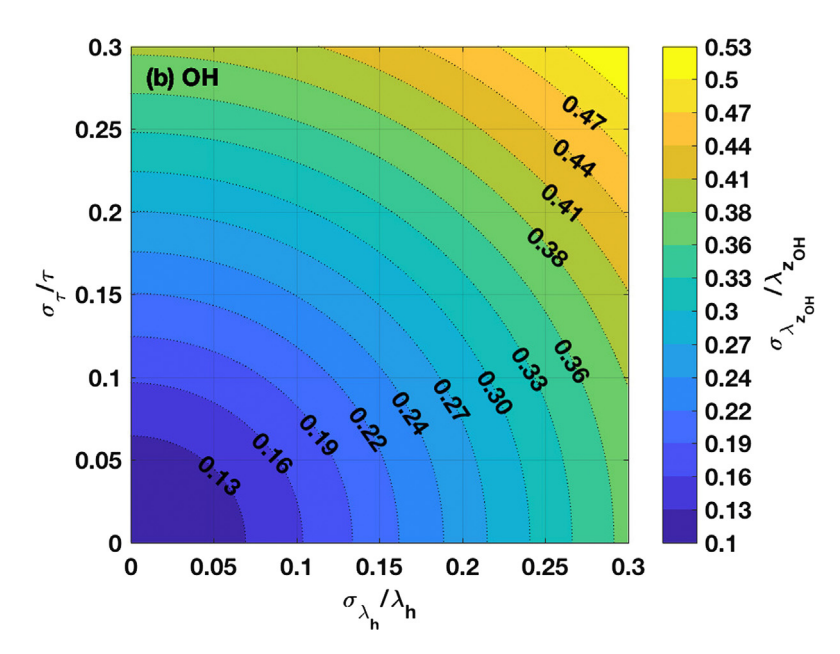


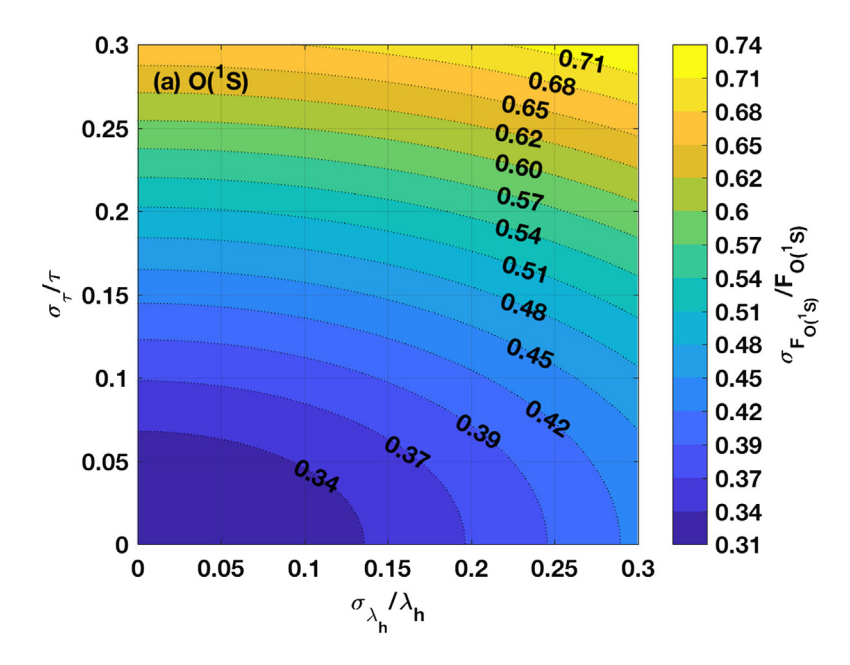
Fig. 9. Relative error in the vertical wavelength as function of  $\sigma_{\lambda_h}/\lambda_h$  and  $\sigma_{\tau}/\tau$ . Input parameters in Eq. (8) to compose (a):  $\lambda_h=100$  km,  $\tau=20$  min,  $\lambda_z=26$  km, N=0.022 rad/s, H=5.4 km,  $\sigma_N/N=0.05$ , and  $\sigma_H/H=0.017$ . Input parameters in Eq. (8) to compose (b):  $\lambda_h=100$  km,  $\tau=20$  min,  $\lambda_z=29.5$  km, N=0.019 rad/s, H=5.6 km,  $\sigma_N/N=0.08$ , and  $\sigma_H/H=0.03$ .

Eq. (17), we have chosen  $\lambda_z \sim 29.5$  km, which correspond to a phase lag of  $\sim 1.5$  rad = 89°. This vertical wave scale is commonly measured by our nightglow image data.

Notice that even  $\sigma_{\Delta z}/\Delta z$  ranges from 0 to 0.6 in the vertical axis of Fig. 12, we know from Zhao et al. (2005) that the relative uncertainty in the vertical separation of night-glow layers is  $\sigma_{\Delta z}/\Delta z \sim 50\%$  due to an uncertainty of  $\sim$ 2.5 km in their centroid altitude. Nonetheless, the error in  $\lambda_z$  grows faster with the uncertainty in  $\Delta \phi$  than with that in  $\Delta z$ . In fact, even though the  $\sigma_{\Delta z}/\Delta z = 0$ , the relative uncertainty in  $\lambda_z$  is still  $\sim$ 60% for a 10% uncertainty in  $\Delta \phi$ , which is quite large from the measurement standpoint.

## 4. Discussion

We have presented in Section 2 the fundamental uncertainties on the parameters  $\lambda_h$ ,  $\theta$ ,  $\tau$ , and I'. These fundamental uncertainties are smaller than 10% and have been measured directly by our nightglow image database (Fig. 8). Remarkably, even the magnitude of these fundamental uncertainties being relatively small, the error propagated to derived quantities as the vertical wavelength, momentum flux and flux divergence become larger than desired. Table 2 presents a summary of the most relevant uncertainties obtained in this study.



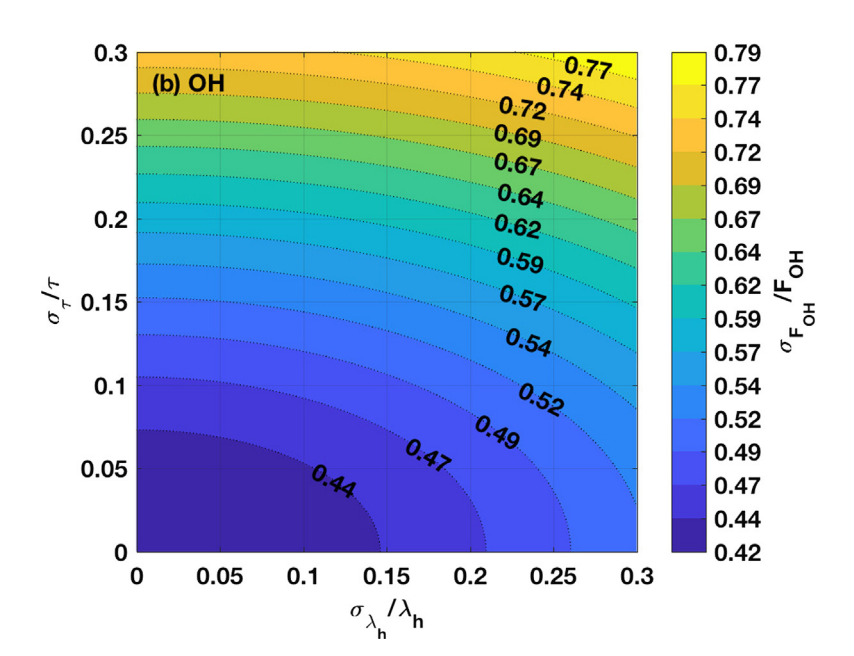


Fig. 10. Relative error on the gravity wave momentum flux in the OH and O( $^1S$ ) layers as function of  $\sigma_{\lambda_h}/\lambda_h$  and  $\sigma_{\tau}/\tau$ . We have considered here a saturated wave of 1% amplitude to compose these charts. Input parameters in Eq. (10) to compose (a):  $\lambda_h = 100$  km,  $\tau = 20$  min,  $\lambda_z = 26$  km, I' = 1%, F = 0.11 m<sup>2</sup>/s<sup>2</sup>,  $\sigma_{I'}/I' = 0.1$ ,  $\sigma_N/N = 0.05$ ,  $\sigma_H/H = 0.017$ ,  $\sigma_{\lambda_z}/\lambda_z = 0.07$ , and  $\sigma_{CF}/CF = 0.04$ . Input parameters in Eq. (10) to compose (b):  $\lambda_h = 100$  km,  $\tau = 20$  min,  $\lambda_z = 29.5$  km, I' = 1%, F = 0.28 m<sup>2</sup>/s<sup>2</sup>,  $\sigma_{I'}/I' = 0.1$ ,  $\sigma_N/N = 0.08$ ,  $\sigma_H/H = 0.03$ ,  $\sigma_{\lambda_z}/\lambda_z = 0.1$ , and  $\sigma_{CF}/CF = 0.07$ .

A key AGW parameter is the momentum flux divergence. For the simulated conditions used in this work, we have shown that the error in D is at least 65% for the background conditions and variations presented in Section 2. As D depends upon 10 variables, it is the most difficult to measure due to the small uncertainties in its parameters propagating into  $\sigma_D$ .

As showed in Fig. 11, the smallest uncertainty in D is still larger than wanted for regular observational conditions, and estimating the flux divergence in a statistically

significant manner requires averaging multiple observations of similar waves, i.e., waves with similar dynamical characteristics. This is analogous to what Gardner and Liu (2007) and Gardner and Liu (2010) have done for heat and constituent flux measurements, which are intrinsically small quantities affected by large uncertainties (mainly caused by photon noise) in lidar measurements. Because of that, many independent instances of these two parameters must be averaged to reduce their uncertainties to acceptable levels.

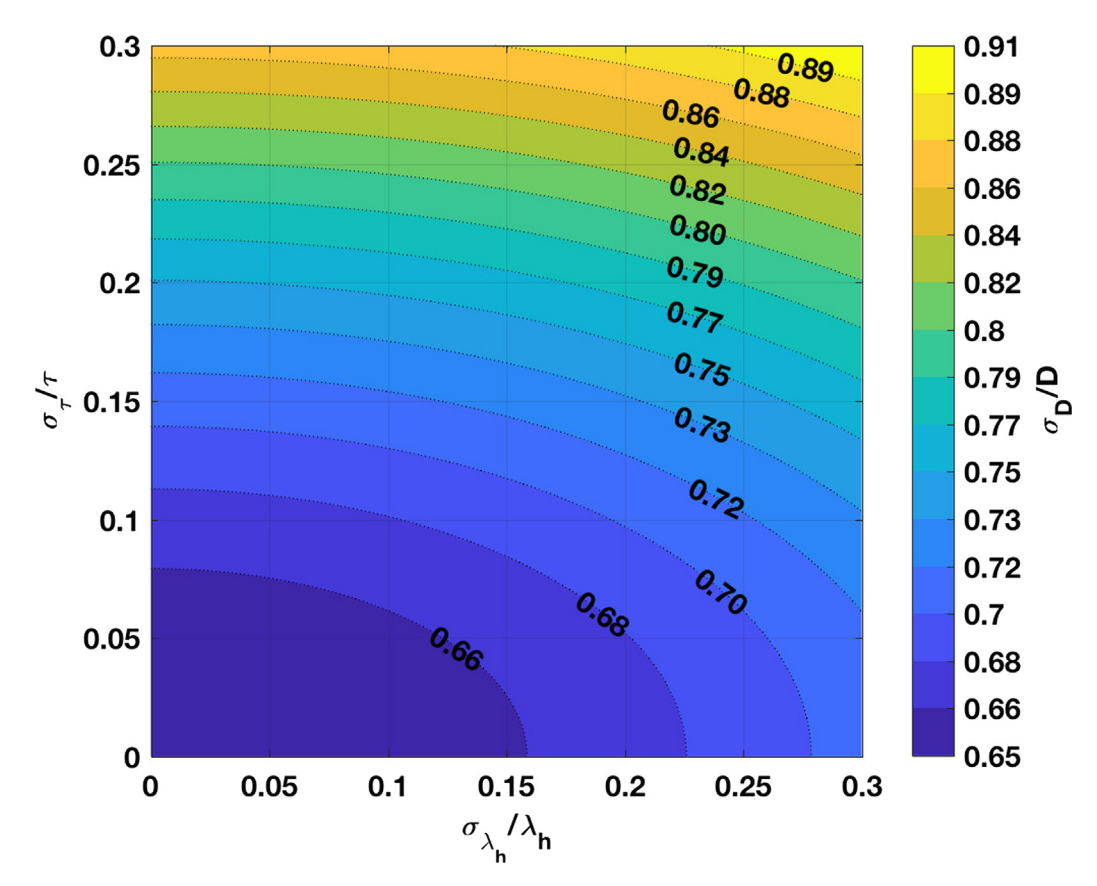


Fig. 11. Relative error on the gravity wave flux divergence as a function of the relative uncertainties in  $\lambda_h$  and  $\tau$ . Input parameters in Eq. (16):  $\lambda_h = 100$  km,  $\tau = 20$  min,  $\lambda_{z_1} = 29.5$  km,  $\lambda_{z_2} = 26$  km, I' = 1%, D = 4.7 m/s/day,  $\sigma_{I'}/I' = 0.1$ ,  $\sigma_{N_1}/N_1 = 0.08$ ,  $\sigma_{N_2}/N_2 = 0.05$ ,  $\sigma_{H_1}/H_1 = 0.03$ ,  $\sigma_{H_2}/H_2 = 0.017$ ,  $\sigma_{\lambda_{z_1}}/\lambda_{z_1} = 0.1$ ,  $\sigma_{\lambda_{z_2}}/\lambda_{z_2} = 0.07$ ,  $\sigma_{CF_1}/CF_1 = 0.07$ ,  $\sigma_{CF_2}/CF_2 = 0.04$ ,  $\sigma_{\rho}/\rho = 0.1$ ,  $\sigma_{\Delta\rho}/\Delta\rho = 0.11$ , and  $\sigma_{\Delta z}/\Delta z = 0.5$ .

In fact, as the standard error  $\sigma_{\overline{D}}$  is given by  $\sigma_{\overline{D}} = \sigma_D/\sqrt{n}$ , where n is the number of independent estimations of D, we will need  $n = (\sigma_D/\sigma_{\overline{D}})^2$  measurements to reduce the error to acceptable uncertainty levels. For example, taking the smaller uncertainty in Fig. 11 as  $\sigma_D = 65\%$ , it would take  $\sim$ 11 independent estimations of D to obtain a single measurement of  $\overline{D}$  with 20% error, even though unrealistically  $\tau$  and  $\lambda_h$  are taken as error-free. An uncertainty of 20% is in agreement with the momentum flux and flux divergence variabilities reported by Ern et al. (2011). On the other hand, we have demonstrated that the relative errors in  $\lambda_h$ and  $\tau$  are nonzero, thus, even more independent measurements of D must be averaged. For a two-week observation campaign, we typically record ~96 h of nightglow image data per month. Assuming that waves having  $\lambda_h = 100$ km and  $\tau = 20$  min occur at a rate of  $\sim 2$  events/hour, we will register 192 events of that type of wave monthly, permitting to make  $\sim 17$  statistical meaningful estimations of  $\overline{D}$  in that particular wave range during the campaign.

Because the observational conditions are not always ideal due to background contamination or due to changes in the occurrence rate of wave events of specific characteristics every night, the variance in D may also vary. In this case, using weighted mean  $\overline{D} = \frac{\sum_{i=1}^n D_i/\sigma_{D_i}^2}{\sum_{i=1}^n 1/\sigma_{D_i}^2}$  and weighted standard deviation  $\sigma_{\overline{D}} = \frac{1}{\sqrt{\sum_{i=1}^n 1/\sigma_{D_i}^2}}$  is ideally better

because small uncertainty, higher accuracy measurements will have a larger influence on the mean and the uncertainty (the standard deviation of the mean). This is better then the arithmetic mean and standard deviation themselves that just ignore the magnitude of the error in each measurement.

Beyond averaging, we can also minimize the D uncertainty by making better estimations of the input variables in the D equation. This can be achieved by having collocated modern Na lidar systems providing high-resolution measurements of temperature and density in the altitude range overlapping the nightglow layers, allowing to calculate N and H more accurately (e.g., Gardner and Liu, 2010; Gardner and Vargas, 2014). Because the lidar error estimations are minimum at  $\sim$ 92 km where the sodium density peaks, the uncertainties in N and H will not be optimum at the OH and  $O(^1S)$  layer altitudes, but will be smaller and more realistic than those obtained here from the NRLMSISE-00 model  $(\sigma_N/N=8\%~(5\%)$  and  $\sigma_H/H=3\%~(2\%)$  at the peak of the OH  $(O(^1S))$  layer).

Similarly, we have shown that the uncertainty in F is quite sensitive to CF because  $\sigma_{CF}$  increases as the vertical wavelength decreases. Additionally, because  $\sigma_{\lambda_z}$  increases as  $\lambda_z$  increases, the uncertainty in F also grows large (Eq. (10)). Our results show that relatively higher precision measurements of F are obtained in the optimum range of  $20 < \lambda_z < 50$  km, but even in this optimum range the error

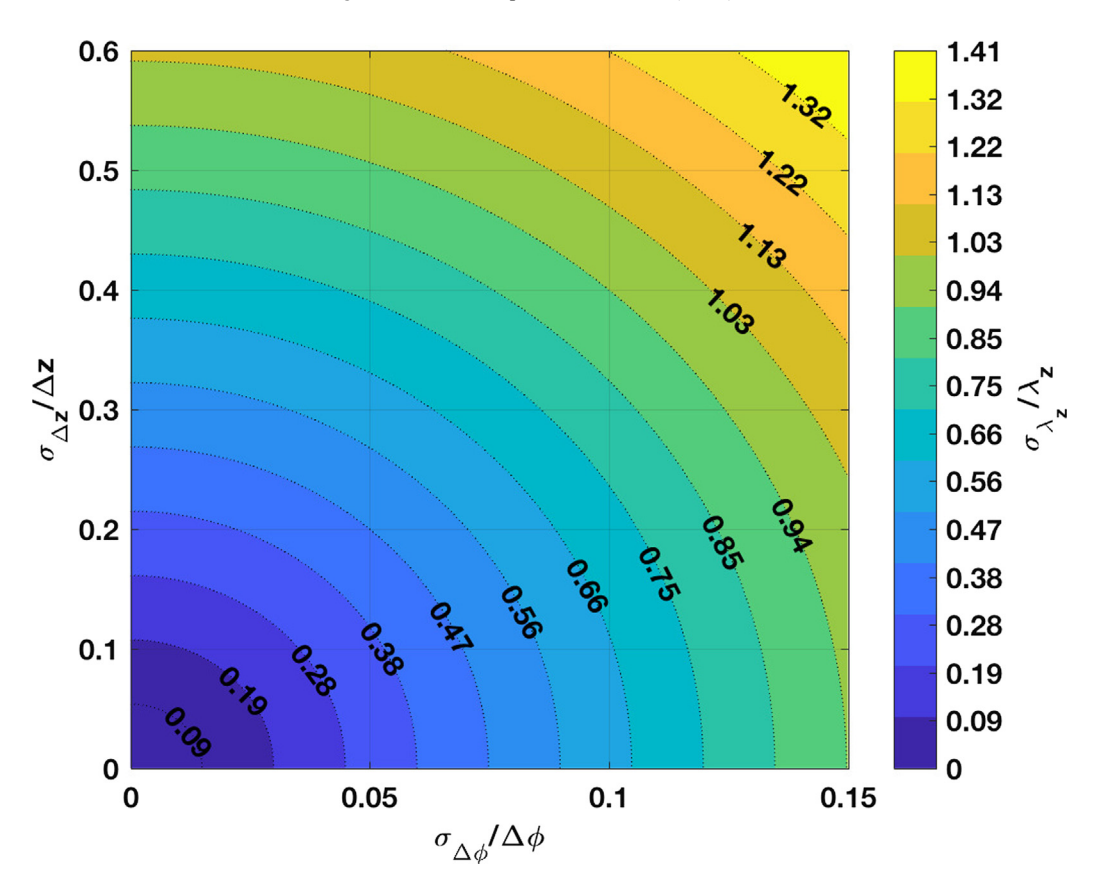


Fig. 12. Error in  $\lambda_z$  due to uncertainties in  $\Delta_z$  and  $\Delta\phi$ . Input parameters in Eq. (18):  $\lambda_z = 29.5$  km,  $\Delta z = 7$  km, and  $\Delta\phi = 1.5$  rad.

Summary of estimated errors in key gravity wave parameters and background quantities. Uncertainties in F,D and m are the smallest for  $\sigma_{\lambda_h} = \sigma_{\tau} = 0$ .

Parameter	Magnitude	Relative uncertainty	Emission	Reference
D	4.7 m/s/day	~65%	_	Eq. (16)
F	$0.3 (0.1) \text{ m}^2/\text{s}^2$	~42% (35%)	OH $(O(^1S))$	Eq. (10)
m	$\frac{2\pi}{29.5} \left(\frac{2\pi}{26}\right) \text{ rad/km}$	~10% (7%)	OH $(O(^1S))$	Eq. (8)
$\lambda_z$	29.5 km	~55%	_	Eq. (18)
I'	0.5–6%	<1%	ОН	Fig. 8c
τ	6–30 min	≲ 10%	ОН	Eq. (3)
$\lambda_h$	20–100 km	$\lesssim 10\%$	ОН	Fig. 8a
N	0.019 (0.022) rad/s	~8% (3%)	OH $(O(^1S))$	Fig. 4d
H	5.6 (5.3) km	~3.5% (2%)	OH $(O(^1S))$	Fig. 4c
[O]	$3\times10^{11} \ (4\times10^{11}) \ cm^{-3}$	~14% (18%)	OH $(O(^1S))$	Fig. 3d
CF	2.8 (4.2)	~6.5% (3.7%)	OH $(O(^1S))$	Eq. (12)
$\Delta z$	7 km	~50%	_	Zhao et al. (2005)

is large, that is,  $\sigma_F/F$  is about 42% (35%) for OH (O( $^1S$ )), at least, assuming zero uncertainties in  $\lambda_h$  and  $\tau$  (Fig. 10). Thus, we show again that averaging several independent estimations is necessary to obtain representative estimations of F (and consequently D).

The error in the vertical wavelength obtained from Eq. (8) is at least  $\sim 10\%$  for OH (8% for O( $^1S$ )) even if the uncertainties in  $\lambda_h$  and  $\tau$  are zero. This is due to nonzero uncertainties in N and H considered in our calculations. Also, notice that because of the thermal and compositional vertical structure of the mesosphere, the magnitudes of N and H at the OH and O( $^1S$ ) layer altitudes differ signifi-

cantly, and the vertical scale of a given wave will be different there. It is clear from our results that N and H cause differences in the magnitude of  $\lambda_z$  at distinct altitudes, which therefore play a significant role on the determination of the momentum flux and the flux divergence as well.

On the other hand, the determination of  $\lambda_z$  from multiple layer observations (Eq. (17)) serve to confirm that one of the dispersion relation when the necessary information is available. This approach requires precise and simultaneous measurements of the wave phase lag ( $\Delta\phi$ ) between the OH and O( $^1S$ ) layers because  $\sigma_{\lambda_z}/\lambda_z$  grows more rapidly with  $\sigma_{\Delta\phi}$  than with  $\sigma_{\Delta z}$  (Fig. 12).

Taori et al. (2007), Takahashi et al. (2011) and Parihar et al. (2013) have measured with good accuracy the phase lag of waves observed in multiple layers using the cosine method applied to photometer datasets. However, estimation of  $\lambda_z$  also depends on the layers separation  $\Delta z$ , which is poorly known because of its large uncertainty. In our estimations, considering that the centroid of a layer could be offset by  $\sim 2.5$  km by tides (see Zhao et al., 2005), the uncertainty in  $\Delta z$  is about 50%. Because of that huge uncertainty in  $\Delta z$ , estimations of  $\lambda_z$  will be subject to errors larger than  $\sim 55\%$ , even if the error in  $\Delta \phi$  is zero (Fig. 12). Fortunately, we can carry out measurements of the centroid altitude of nightglow layers through the triangulation technique (e.g., Kubota et al., 1999; Ejiri et al., 2002), which represents a viable way to reduce the uncertainty in  $\Delta z$ .

As our simulation algorithm permits to turn on/off error sources separately as needed, we have evaluated the significance of each error source in some of the uncertainty equations presented here. For example, the dominant error source in vertical wavenumber (Eq. (8)) is due to N, which correspond to 99.7% of the total variance in  $\lambda_z$  when the uncertainties in  $\tau$  and  $\lambda_h$  are small. This way,  $\sigma_H$  is negligible and H can be taken as constant throughout the MLT.

Larger errors sources in the momentum flux are due to I' and N, which respond to 42% and 46.7% of the total variance in F (Eq. (10)), respectively. The error in F caused by m and CF correspond to only 5.6% and 5.8% of total F variance (assuming  $\lambda_z = 29.5$  km).

Error sources associated with  $\bar{\rho}$  and  $\Delta \bar{\rho}$  play a very small role in Eq. (16), responding to only 0.8% and 0.6% of the total variance in D, respectively, and can be safely neglected. The uncertainty in D depends critically on  $\Delta z$  error, which corresponds to  $\sim$ 61% of the total D variance, while  $\sigma_{\Delta F}$  and  $\sigma_{F}$  terms cause, respectively, 25.5% and 11.8% of the total variance in D under the simulated conditions of this study.

Having lidar temperature data available lowers the error in T to less than 1% in the altitude range of 85–100 km. The derived quantities N and H would have similar uncertainties, but errors in the vertical wavelength would decrease from 21% to 18%, errors in the momentum flux would decrease from 49% to 30%, and errors in the flux divergence would be lowered from 68% to 58%, assuming errors of about 10% in both in the horizontal wavelength and in the wave period.

Regarding the cancellation factor, there are intrinsic assumptions made in our model that must be pointed out here. We have assumed an isothermal and windless atmosphere where the influence of wind shear, temperature gradients, and turbulence, were disregarded. Gardner and Vargas (2016) have studied the impact of turbulent structures on OH nightglow images and have found that only larger eddies would be captured in nightglow images in nights when the environmental eddy diffusion coefficient  $k_{zz}$  becomes unusually large. That would explain the low

observation rate of breaking AGWs events observed by our nightglow imager, and also would support our approach here where we consider a non-turbulent MLT, once turbulence cannot be seen easily by such an ordinary nightglow imagery device once the filter wheel cycle is too long to resolve the turbulence structures properly (Gardner and Vargas, 2016). To observe fine turbulence structures, it would be necessary a dedicated, single emission all-sky imager that would allow decreasing the integration times to 15 s using wide band interference filters to observe, for instance, the OH emission with good signal-to-noise ratio images.

Additionally, Hickey and Yu (2005) have assessed via a full wave model the consequences on CF when a structured MLT is present. According to their results, the cancellation factor could change by a factor of two due to the thermal MLT structure (non-isothermal mean state) and also by another factor of two due to the nonzero wind structure (but only for waves presenting phase velocities larger than 100 m/s). Consequently, according to Hickey and Yu (2005), eddy diffusion is not important for the slowest gravity waves, and its effect only occurs for very fast gravity waves that are not usually observed in the nightglow (Hickey and Yu, 2005). Thus, our CF model is compatible with that of Hickey and Yu (2005) in the phase velocity range of 50 to 100 m/s.

Finally, uncertainties in *CF* also depend critically on the altitude distribution of the atomic oxygen, a major player in the nightglow chemistry that varies considerably with latitude and time. Thus, [O] should be readily available from observational sources once realistic changes in [O] are not captured in the NRLMSISE-00 model used here in estimations of the *CF* variability.

#### 5. Conclusion

We have presented in this paper a comprehensive discussion about the magnitude of the uncertainties in gravity wave parameters estimated from nightglow measurements, and how these uncertainties affect the estimation of key dynamic quantities in the MLT. Because of uncertainties in fundamental wave parameters and in environmental quantities, derived AGW parameters such as the vertical wavelength, the momentum flux and the gravity wave flux divergence are subject to large uncertainties.

The least quantified error sources of the gravity wave dynamics are associated with N and  $\Delta z$ . Because these errors sources critically influence the AGW derived quantities, future experimental schemes must be devised to minimize the errors in N and  $\Delta z$  if statistically meaningful estimations are to be made from nightglow observations. Error sources associated with the scale height and with the background density play only minor roles on the uncertainty of the derivable parameters and can be neglected. The remaining error sources of the AGW dynamics are either well known or can be determined accurately.

We have shown that the uncertainty in the momentum flux depends critically on  $\lambda_z$  and CF. Measurements of F have a smaller error in the range of 20–50 km vertical wavelength. Out of that optimum range, the uncertainty in F grows rapidly because of the uncertainties in CF (for  $\lambda_z < 20$  km) and in  $\lambda_z$  (for  $\lambda_z > 50$  km) become unbearably large.

However, uncertainties in both the momentum flux and flux divergence are large even in the optimum  $\lambda_z$  range, which are only minimized upon averaging multiple independent measurements of these quantities. To access to their absolute uncertainties, we recommend using the weighted mean and weighted standard deviation to make ideally better estimations of F and D than those provided by the arithmetic mean and standard deviation.

The equations presented in Section 2 are simple enough and we encourage their use by other aeronomers working on gravity wave studies. As many research groups rely on similar AGW parameter estimation schemes, the errors calculation procedures discussed here can be implemented to image processing routines straightforwardly.

#### Acknowledgments

This work has been supported by the National Science Foundation under Grant # 11-36208 and Grant # 11-15725. We also acknowledge three unrevealed reviewers for their valuable contribution to the present work. Andes Lidar Observatory image data supporting Fig. 8 are available under email request to the authors.

#### References

- Batista, P.P., Clemesha, B.R., Simonich, D.M., Taylor, M.J., Takahashi, H., Gobbi, D., Batista, I.S., Buriti, R.A., de Medeiros, A.F., 2002. Simultaneous lidar observation of a sporadic sodium layer, a "wall" event in the OH and OI5577 airglow images and the meteor winds. J. Atmos. Solar Terr. Phys. 64 (12–14), 1327–1335. https://doi.org/10.1016/S1364-6826(02)00116-5.
- Bevington, P.R., Robinson, D.K., 1969. Data Reduction and Error Analysis for the Physical Sciences, vol. 336. McGraw-Hill, New York. Chamberlain, J.W., 1995. Physics of the Aurora and Airglow, vol. 41.
- American Geophysical Union.

  Coble, M., Papen, G., Gardner, C., 1998. Computing two-dimensional unambiguous horizontal wavenumber spectra from oh airglow images.
- unambiguous horizontal wavenumber spectra from oh airglow images. IEEE Trans Geosci. Remote Sens. 36 (2), 368–382. https://doi.org/10.1109/36.662723.
- Ejiri, M.K., Shiokawa, K., Ogawa, T., Kubota, M., Nakamura, T., Tsuda, T., 2002. Dual-site imaging observations of small-scale wave structures through OH and OI nightglow emissions. Geophys. Res. Lett. 29 (10), 85-1–85-4. https://doi.org/10.1029/2001GL014257.
- Ern, M., Preusse, P., Gille, J.C., Hepplewhite, C.L., Mlynczak, M.G., Russell, J.M., Riese, M., 2011. Implications for atmospheric dynamics derived from global observations of gravity wave momentum flux in stratosphere and mesosphere. J. Geophys. Res.: Atmos. 116 (D19). https://doi.org/10.1029/2011JD015821.
- Garcia, F.J., Taylor, M.J., Kelley, M.C., 1997. Two-dimensional spectral analysis of mesospheric airglow image data. Appl. Opt. 36 (29), 7374– 7385. https://doi.org/10.1364/AO.36.007374.
- Gardner, C.S., Liu, A.Z., 2007. Seasonal variations of the vertical fluxes of heat and horizontal momentum in the mesopause region at Starfire

- Optical Range, New Mexico. J. Geophys. Res.: Atmos. 112 (D9). https://doi.org/10.1029/2005JD006179.
- Gardner, C.S., Liu, A.Z., 2010. Wave-induced transport of atmospheric constituents and its effect on the mesospheric Na layer. J. Geophys. Res.: Atmos. 115 (D20). https://doi.org/10.1029/2010JD014140.
- Gardner, C.S., Taylor, M.J., 1998. Observational limits for lidar, radar, and airglow imager measurements of gravity wave parameters. J. Geophys. Res.: Atmos. 103 (D6), 6427–6437. https://doi.org/10.1029/97JD03378.
- Gardner, C.S., Vargas, F.A., 2014. Optimizing three-frequency Na, Fe, and He lidars for measurements of wind, temperature, and species density and the vertical fluxes of heat and constituents. Appl. Opt. 53 (19), 4100–4116. https://doi.org/10.1364/AO.53.004100.
- Gardner, C.S., Vargas, F.A., 2016. OH\* imager response to turbulence-induced temperature fluctuations. J. Geophys. Res.: Atmos. 121 (23), 13,919–13,935. https://doi.org/10.1002/2016JD025453.
- Gardner, C.S., Voelz, D.G., 1987. Lidar studies of the nighttime sodium layer over Urbana, Illinois: 2. Gravity waves. J. Geophys. Res.: Space Phys. 92 (A5), 4673–4694. https://doi.org/10.1029/JA092iA05p04673.
- Giers, D., Sahai, Y., Cogger, L., Ryan, E., 1997. Occurrence characteristics of mesospheric gravity waves at 51°N. J. Atmos. Solar Terr. Phys. 59 (10), 1197–1203. https://doi.org/10.1016/S1364-6826(96) 00117-4.
- Hapgood, M., Taylor, M.J., 1982. Analysis of airglow image data. Ann. Geophys. 38 (805–813).
- Hecht, J.H., Walterscheid, R.L., Ross, M.N., 1994. First measurements of the two-dimensional horizontal wave number spectrum from ccd images of the nightglow. J. Geophys. Res.: Space Phys. 99 (A6), 11,449–11,460. https://doi.org/10.1029/94JA00584.
- Hickey, M.P., Yu, Y., 2005. A full-wave investigation of the use of a "cancellation factor" in gravity wave-oh airglow interaction studies. J. Geophys. Res.: Space Phys. 110 (A1). https://doi.org/10.1029/ 2003JA010372.
- Hines, C., 1960. Internal atmospheric gravity waves at ionospheric heights. Can. J. Phys. 38 (11), 1441–1481.
- Hocking, W.K., 2005. A new approach to momentum flux determinations using SKiYMET meteor radars. Ann. Geophys. 23 (7), 2433–2439. https://doi.org/10.5194/angeo-23-2433-2005.
- Krassovsky, V.I., 1972. Infrasonic variations of OH-emission in upper-atmosphere. Ann. Geophys. 28 (4), 739–746.
- Kubota, M., Ishii, M., Shiokawa, K., Ejiri, M., Ogawa, T., 1999. Height measurements of nightglow structures observed by all-sky imagers. Adv. Space Res. 24 (5), 593–596. https://doi.org/10.1016/S0273-1177 (99)00206-9.
- Li, Z., Liu, A.Z., Lu, X., Swenson, G.R., Franke, S.J., 2011. Gravity wave characteristics from OH airglow imager over Maui. J. Geophys. Res.: Atmos. 116 (D22). https://doi.org/10.1029/2011JD015870.
- Liu, A.Z., Swenson, G.R., 2003. A modeling study of o2 and oh airglow perturbations induced by atmospheric gravity waves. J. Geophys. Res.: Atmos. 108 (D4). https://doi.org/10.1029/2002JD002474.
- Lu, X., Liu, A.Z., Swenson, G.R., Li, T., Leblanc, T., McDermid, I.S., 2009. Gravity wave propagation and dissipation from the stratosphere to the lower thermosphere. J. Geophys. Res.: Atmos. 114 (D11). https://doi.org/10.1029/2008JD010112.
- McCormac, B.M., 1967, Aurora and airglow. In: Aurora and Airglow, vol. 1.
- Meriwether, J.W., 1989. A review of the photochemistry of selected nightglow emissions from the mesopause. J. Geophys. Res.: Atmos. 94 (D12), 14,629–14,646. https://doi.org/10.1029/JD094iD12p14629.
- Nappo, C., 2012. An Introduction to Atmospheric Gravity Waves International Geophysics. Elsevier Science.
- Nikoukar, R., Swenson, G.R., Liu, A.Z., Kamalabadi, F., 2007. On the variability of mesospheric OH emission profiles. J. Geophys. Res.: Atmos. 112 (D19). https://doi.org/10.1029/2007JD008601.
- Offermann, D., Friedrich, V., Ross, P., Zahn, U.V., 1981. Neutral gas composition measurements between 80 and 120 km. Planet. Space Sci. 29 (7), 747–764. https://doi.org/10.1016/0032-0633(81)90046-5.

- Parihar, N., Taori, A., Gurubaran, S., Mukherjee, G.K., 2013. Simultaneous measurement of OI 557.7 nm, O<sub>2</sub> (0, 1) atmospheric band and OH (6, 2) Meinel band nightglow at Kolhapur 17° N, India. Ann. Geophys. 31 (2), 197–208. https://doi.org/10.5194/angeo-31-197-2013.
- Pautet, P.-D., Taylor, M.J., Liu, A.Z., Swenson, G.R., 2005. Climatology of short-period gravity waves observed over northern Australia during the Darwin Area Wave Experiment (DAWEX) and their dominant source regions. J. Geophys. Res.: Atmos. 110 (2). https://doi.org/ 10.1029/2004JD004954.
- Picone, J.M., Hedin, A.E., Drob, D.P., Aikin, A.C., 2002. NRLMSISE-00 empirical model of the atmosphere: statistical comparisons and scientific issues. J. Geophys. Res: Space Phys. 107 (A12). https://doi.org/10.1029/2002JA009430, SIA 15-1–SIA 15-16.
- Reisin, E.R., Scheer, J., 1996. Characteristics of atmospheric waves in the tidal period range derived from zenith observations of O2(0-1) atmospheric and OH(6-2) airglow at lower midlatitudes. J. Geophys. Res.: Atmos. 101 (D16), 21,223-21,232. https://doi.org/10.1029/96ID01773
- Shepherd, G.G., Thuillier, G., Solheim, B.H., Chandra, S., Cogger, L.L., Duboin, M.L., Evans, W.F.J., Gattinger, R.L., Gault, W.A., Hersé, M., Hauchecorne, A., Lathuilliere, C., Llewellyn, E.J., Lowe, R.P., Teitelbaum, H., Vial, F., 1993. Longitudinal structure in atomic oxygen concentrations observed with WINDII on UARS. Geophys. Res. Lett. 20 (12), 1303–1306. https://doi.org/10.1029/93GL01105.
- Swenson, G.R., Gardner, C.S., 1998. Analytical models for the responses of the mesospheric OH\* and Na layers to atmospheric gravity waves. J. Geophys. Res.: Atmos. 103 (D6), 6271–6294. https://doi.org/10.1029/ 97JD02985.
- Swenson, G.R., Liu, A.Z., 1998. A model for calculating acoustic gravity wave energy and momentum flux in the mesosphere from OH airglow. Geophys. Res. Lett. 25 (4), 477–480. https://doi.org/10.1029/ 98GL00132.
- Swenson, G.R., Mende, S.B., 1994. OH emission and gravity waves (including a breaking wave) in all-sky imagery from Bear Lake, UT. Geophys. Res. Lett. 21 (20), 2239–2242. https://doi.org/10.1029/94GL02112.
- Swenson, G.R., Haque, R., Yang, W., Gardner, C.S., 1999. Momentum and energy fluxes of monochromatic gravity waves observed by an OH imager at Starfire Optical Range, New Mexico. J. Geophys. Res.: Atmos. 104 (D6), 6067–6080. https://doi.org/10.1029/1998JD200080.
- Swenson, G., Yee, Y., Vargas, F., Liu, A., 2018. Vertical diffusion transport of atomic oxygen in the mesopause region consistent with chemical losses and continuity: global mean and inter-annual vari-

- ability. J. Atmos. Sol.-Terr. Phys. https://doi.org/10.1016/j.jastp.2018.05.014.
- Takahashi, H., Onohara, A., Shiokawa, K., Vargas, F., Gobbi, D., 2011. Atmospheric wave induced O<sub>2</sub> and OH airglow intensity variations: effect of vertical wavelength and damping. Ann. Geophys. 29 (4), 631–637. https://doi.org/10.5194/angeo-29-631-2011.
- Tang, J., Liu, A.Z., Swenson, G.R., 2002. High frequency gravity waves observed in OH airglow at Starfire Optical Range, NM: seasonal variations in momentum flux. Geophys. Res. Lett. 29 (20), 27-1–27-4. https://doi.org/10.1029/2002GL015794.
- Tang, J., Kamalabadi, F., Franke, S.J., Liu, A., Swenson, G., 2005a. Estimation of gravity wave momentum flux with spectroscopic imaging. IEEE Trans. Geosci. Remote Sens. 43 (1), 103–109. https:// doi.org/10.1109/TGRS.2004.836268.
- Tang, J., Swenson, G.R., Liu, A.Z., Kamalabadi, F., 2005b. Observational investigations of gravity wave momentum flux with spectroscopic imaging. J. Geophys. Res.: Atmos. 110 (D9). https://doi.org/10.1029/2004JD004778.
- Taori, A., Guharay, A., Taylor, M.J., 2007. On the use of simultaneous measurements of OH and O<sub>2</sub> emissions to investigate wave growth and dissipation. Ann. Geophys. 25 (3), 639–643. https://doi.org/10.5194/angeo-25-639-2007.
- Taylor, M.J., Pendleton, W.R., Clark, S., Takahashi, H., Gobbi, D., Goldberg, R.A., 1997. Image measurements of short-period gravity waves at equatorial latitudes. J. Geophys. Res.: Atmos. 102 (D22), 26,283–26,299. https://doi.org/10.1029/96JD03515.
- Vargas, F., Swenson, G., Liu, A., Gobbi, D., 2007. O(\dangle S), OH, and O2(b) airglow layer perturbations due to AGWs and their implied effects on the atmosphere. J. Geophys. Res.: Atmos. 112 (D14). https://doi.org/10.1029/2006JD007642.
- Vargas, F., Gobbi, D., Takahashi, H., Lima, L.M., 2009. Gravity wave amplitudes and momentum fluxes inferred from oh airglow intensities and meteor radar winds during SpreadFEx. Ann. Geophys. 27 (6), 2361–2369. https://doi.org/10.5194/angeo-27-2361-2009.
- Vargas, F., Swenson, G., Liu, A., 2015. Evidence of high frequency gravity wave forcing on the meridional residual circulation at the mesopause region. Adv. Space Res. 56 (9), 1844–1853. https://doi.org/10.1016/j. asr.2015.07.040.
- Weeks, A.R., 1996. Fundamentals of Electronic Image Processing. SPIE Optical Engineering Press Bellingham.
- Zhao, Y., Taylor, M.J., Chu, X., 2005. Comparison of simultaneous Na lidar and mesospheric nightglow temperature measurements and the effects of tides on the emission layer heights. J. Geophys. Res.: Atmos. 110 (D9). https://doi.org/10.1029/2004JD005115.